

TECHNICAL
MEMORANDUM

NCSC TM-275-79

NOVEMBER 1979

12
3

ADA 079491

A WAVE-SPACE MODEL
FOR ACOUSTIC SCATTERING
FROM ELASTIC CYLINDERS

J.C. NELANDER

Approved for public release;
distribution-unlimited

DDC
RECEIVED
JAN 17 1980
RECEIVED
A

DDC FILE COPY



NAVAL COASTAL SYSTEMS CENTER

NCSC

PANAMA CITY, FLORIDA

32407



BEST
AVAILABLE COPY

copy 59

80-

035



NAVAL COASTAL SYSTEMS CENTER

PANAMA CITY, FLORIDA

32407

CAPT RAYMOND D. BENNETT, USN
Commanding Officer

GERALD G. GOULD
Technical Director

ADMINISTRATIVE INFORMATION

The memorandum describes work accomplished on Task 00112-60 of Task Area No. ZF 61112001, *Target Broadband Scattering Characteristics*, over the period 1 September 1977 through 1 March 1979. This work, sponsored by NCSC IED, represents a portion of a continuing effort in the analysis of acoustic scattering by elastic targets. A more extensive account of this work, including computer programs, may be found ^{WA} in NCSC Technical Note 477, March 1979. The author wishes to acknowledge the helpful comments of Mr. Don Folds, Dr. David Skinner and Dr. David Vasholz and the contributions of Dr. Chester Loggins, Mr. Sam Richardson, Mrs. Susan Tuovila, Mr. Tim Singleton and Mr. Dan Kimmel.

Released by
Donald L. Folds, Head
High Definition Sonar
Technology Division
November 1979

Under Authority of
M. J. Wynn, Head
Coastal Technology Department

UNCLASSIFIED

SECURITY CLASSIFICATION OF THIS PAGE (When Data Entered)

REPORT DOCUMENTATION PAGE		READ INSTRUCTIONS BEFORE COMPLETING FORM	
1. REPORT NUMBER NCSC-TM-275-79	2. GOVT ACCESSION NO.	3. RECIPIENT'S CATALOG NUMBER	
4. TITLE (and Subtitle) A WAVE-SPACE MODEL FOR ACOUSTIC SCATTERING FROM ELASTIC CYLINDERS		5. TYPE OF REPORT & PERIOD COVERED Technical Memorandum	
7. AUTHOR(s) J. C./Nelander		6. PERFORMING ORG. REPORT NUMBER	
9. PERFORMING ORGANIZATION NAME AND ADDRESS Naval Coastal Systems Center Panama City, Florida 32407		8. CONTRACT OR GRANT NUMBER(s)	
10. PROGRAM ELEMENT, PROJECT, TASK AREA & WORK UNIT NUMBERS Task 00112-60 Task Area ZF 61112001		11. CONTROLLING OFFICE NAME AND ADDRESS 1274	
11. CONTROLLING OFFICE NAME AND ADDRESS		12. REPORT DATE Nov 79	
14. MONITORING AGENCY NAME & ADDRESS (if different from Controlling Office) Technical memo, 1 Sep 77 - 1 Mar 79		13. NUMBER OF PAGES 71	
16. DISTRIBUTION STATEMENT (of this Report) Approved for public release; distribution unlimited.		15. SECURITY CLASS. (of this report) UNCLASSIFIED	
17. DISTRIBUTION STATEMENT (of the abstract entered in Block 20, if different from Report)		15a. DECLASSIFICATION/DOWNGRADING SCHEDULE N/A	
18. SUPPLEMENTARY NOTES 627664			
19. KEY WORDS (Continue on reverse side if necessary and identify by block number) Acoustic scattering Identifiers: Acoustic modeling Elastic cylinders Plane wave scattering Minelike target Impedance boundary			
20. ABSTRACT (Continue on reverse side if necessary and identify by block number) Starting from the wave equation, a formalism for acoustic scattering from minelike targets is derived. A spatial Fourier transform relationship between the target characteristic function and the Fourier or wave-space structure factor is discussed and illustrated. An empirical, plane-wave model for scattering from a finite right circular cylinder is derived. Impedance boundary conditions are incorporated into the model for the cylinder.			

DD FORM 1 JAN 73 1473

EDITION OF 1 NOV 65 IS OBSOLETE
S/N 0102-LF-014-6601

440 650 UNCLASSIFIED
SECURITY CLASSIFICATION OF THIS PAGE (When Data Entered)

REPORT DOCUMENTATION PAGE		READ INSTRUCTIONS BEFORE COMPLETING FORM
1. REPORT NUMBER	2. GOVT ACCESSION NO.	3. RECIPIENT'S CATALOG NUMBER
4. TITLE (and Subtitle)	5. TYPE OF REPORT & PERIOD COVERED	
	6. PERFORMING ORG. REPORT NUMBER	
7. AUTHOR(s)	8. CONTRACT OR GRANT NUMBER(s)	
9. PERFORMING ORGANIZATION NAME AND ADDRESS	10. PROGRAM ELEMENT, PROJECT, TASK AREA & WORK UNIT NUMBERS	
11. CONTROLLING OFFICE NAME AND ADDRESS	12. REPORT DATE	
	13. NUMBER OF PAGES	
14. MONITORING AGENCY NAME & ADDRESS (if different from Controlling Office)	15. SECURITY CLASS. (of this report)	
	15a. DECLASSIFICATION/DOWNGRADING SCHEDULE	
16. DISTRIBUTION STATEMENT (of this Report)		
17. DISTRIBUTION STATEMENT (of the abstract entered in Block 20, if different from Report)		
18. SUPPLEMENTARY NOTES		
19. KEY WORDS (Continue on reverse side if necessary and identify by block number)		
20. ABSTRACT (Continue on reverse side if necessary and identify by block number)		

2 1 1 1	By Distribution Availability Codes Avail and/or Special Dist
------------------	--

TABLE OF CONTENTS

	<u>Page No.</u>
SECTION I - INTRODUCTION.	1
Purpose and Scope.	1
Previous Work and Phenomenology.	2
SECTION II - GENERAL SCATTERING THEORY.	4
SECTION III - EMPIRICAL SCATTERING MODEL.	10
SECTION IV - REAL SPACE - WAVE SPACE RELATIONSHIPS.	15
Ewald Construction	17
Inclination Factor	19
SECTION V - RIGID CYLINDER SCATTERING - FIRST LEVEL APPROXIMATION	22
General Approach	22
Cylinder End Disc Structure Factor	24
Cylinder Side Surface Structure Factor	27
Combined Structure Factor.	31
SECTION VI - RIGID CYLINDER SCATTERING CROSS SECTION.	32
SECTION VII - IMPEDANCE BOUNDARY CONDITION.	41
General Considerations	41
End Disc Reflection Coefficient.	44
Hemi-Cylinder Reflection Coefficient	46

TABLE OF CONTENTS (CONT'D)

	<u>Page No.</u>
Hemi-Cylinder Structure Factor.	49
Complex Values of the Reflection Coefficients	49
SECTION VIII - IMPEDANCE CYLINDER SCATTERING CROSS SECTION.	55
SECTION IX - SUMMARY AND CONCLUSIONS	66

RE: Distribution Statement-
Distribution Unlimited per Dr. J. C.
Nelander, Naval Coastal Systems Center

LIST OF ILLUSTRATIONS

<u>Figure No.</u>		<u>Page No.</u>
1	Scattering Geometry	5
2	Real Space - Wave Space Relationship	16
3	Ewald Construction	18
4	Inclination Factor ($\vec{k} \cdot \hat{n} / \vec{k} $) Relationships	21
5	Geometry for Scattering from a Rigid, Right Circular Cylinder	23
6	Cylinder End Disc (S_1)	26
7	Cylinder Side Surface (S_2)	28
8	Rigid Cylinder Scattering Cross-Section	33
9	Shaded Contour Plot Showing the Four Quadrants of the Rigid Cylinder Scattering Cross-Section	34
10a	Alternate View of the Rigid Cylinder Scattering Cross-Section (Logarithmic Ordinate)	37
10b	Linear Plot Showing the Rayleigh Region of the Rigid Cylinder Scattering Cross-Section	38
11	A Compressional Plane Wave, \vec{k}_A , in a Fluid Half Space is Reflected from a Fluid-Solid Interface into the Direction \vec{k}_B and Refracted into the Solid Half Space in the Form of a Compressional Wave, \vec{k}_D , and a Shear Wave, \vec{k}_E	42
12	Relationship Between the Scattering Vector \vec{k} and the Vector (\hat{n}) Normal to the Hemi-Cylinder Surface at the Point P(x,y,o)	47
13	Reflection Coefficient (a) Modulus, and (b) Phase Angle for Brass in Water	51
14	Reflection Coefficient (a) modulus, and (b) Phase Angle for Aluminum in Water	52

LIST OF ILLUSTRATIONS (CONT'D)

<u>Figure No.</u>		<u>Page No.</u>
15	Reflection Coefficient (a) Modulus, and (b) Phase Angle for Aluminum in Air	53
16	Scattering Cross-Section for an Aluminum Cylinder in Air	56
17	Scattering Cross-Section for an Aluminum Cylinder in Water	58
18	Alternate View of the Scattering Cross-Section for an Aluminum Cylinder in Water	59
19	Shaded Contour Plot for the Scattering Cross-Section for an Aluminum Cylinder in Water	60
20	Scattering Cross-Section for a Brass Cylinder in Water	62
21	Alternate View of the Scattering Cross-Section for a Brass Cylinder in Water	63
22	Shaded Contour Plot of the Scattering Cross-Section for a Brass Cylinder in Water	64

SECTION I

INTRODUCTION

PURPOSE AND SCOPE

Because of the elastic properties of most acoustic targets, the temporal echoes and frequency characteristics of even the simplest targets are distinctive but confusingly complex. These same effects can influence acoustic images as well. Any useful target classification algorithm, via temporal or image processing, should be based upon meaningful target scattering characteristics. Hence, the frequency response, or differential scattering cross-section, of targets of interest need to be measured and understood so that it may guide pattern recognition procedures to those frequency domains which present the most consistent and distinctive features. Once these features have been identified, a waveform may be designed to maximize the desired response.

The purpose of this report is to present both mathematical and heuristic descriptions of acoustic scattering which will be useful in the interpretation of experimental scattering data from minelike objects by providing physical insight toward understanding their origin and significance. Subsequent reports will deal with the results of experimental measurements and their interpretation.

This report is organized into nine sections. In addition to these introductory remarks, Section I contains a brief description of previous work in acoustic scattering and the phenomenology involved. Section II is a derivation of the general scattering theory from the wave equation to the general Kirchhoff diffraction equation. This derivation is included for continuity and completeness. Section III is concerned with the development of an original empirical scattering model based upon a basis set of plane waves and target surface distribution coefficients. Section IV deals with a method of presenting and interpreting scattering data in terms of real-space and wave (or Fourier)-space functions. Section V presents a derivation of a first level approximation to scattering from a rigid, finite cylinder from arbitrary aspect angle, using the empirical model described in Section III. Section VI contains graphical displays of the scattering function derived in Section V as well as comments on the characteristics of the plotted function. Section VII considers impedance boundary conditions for elastic targets. Reflection coefficients for the finite cylinder are derived in terms of the wave-space and real-space parameters of the empirical model. Section VIII contains plots of the finite, impedance cylinder (aluminum and brass) in water as well as a comparison of that for an aluminum cylinder in air with that of the rigid cylinder (Section VI). Section IX concludes with a summary of the empirical model and its utility.

PREVIOUS WORK AND PHENOMENOLOGY

Acoustic scattering measurements for simple targets have been published in the form of time series (temporal) signals for short pulses¹ or as power spectra (frequency domain) of the scattered signal.^{2,3,4,5} The backscattering experimental configuration has been the principal method. Spheres and "infinite" cylinders, from beam aspect, have been the principal targets because their symmetry permits a minimum number of measurements because of the absence of aspect dependence. Some early work^{1,6} shows target directivity patterns in the form of polar plots at discrete frequencies. In these investigations, the acoustic projector and target were held fixed while the receiving hydrophone was rotated about the axis of symmetry of the target. Hence these results show a variation of target response due to changing the experimental geometry (bistatic angle) but not because of the target's geometry or aspect dependence. Little work has been reported which combines the variation of the target response with respect to frequency and target aspect for either backscattering or bistatic angle experimental configurations.

Dunsiger⁷ has examined the aspect dependence of a variety of simple shapes using short pulses at high frequency, where frequency dependence of the target response was assumed to be unimportant. The resulting

¹Barnard, G. R. and McKinney, C. M., "Scattering of Acoustic Energy by Solid and Air Filled Cylinders in Water," J. Acoustic. Soc. Am. 33, 226-238 (1961).

²Hickling, R., "Analysis of Echoes from a Solid Elastic Sphere in Water," J. Acoust. Soc. Am. 34, 1582-1592 (1962).

³Diercks, K. J. and Hickling, R., "Echoes from Hollow Aluminum Spheres in Water," J. Acoust. Soc. Am. 41, 380-393 (1966).

⁴Shirley, D. J. and Diercks, K. J., "Analysis of the Frequency Response of Simple Geometric Targets," ARL-TM-69-21, The University of Texas at Austin, 45 pp. (1970).

⁵Neubauer, W. G., Vogt, R. H., and Dragonette, L. R., "Acoustic Reflection from Elastic Spheres. I. Steady-State Signals," J. Acoust. Soc. Am. 55, 1123-1129 (1974).

⁶Faran, J. J., "Sound Scattering by Solid Cylinders and Spheres," J. Acoust. Soc. Am. 23, 405-418 (1951).

⁷Dunsiger, A. D., "High-Frequency Acoustic Echoes Received From Simple Geometric Shapes with Possible Applications to Target Recognition," J. Sound Vib. 13, 323-345 (1970).

target echoes were a sequence of pulses whose spacing corresponded to the distance between edges and corners of the target as viewed from the projector's line of sight.

Neubauer and Dragonette⁸ have investigated the nature of the wave-field scattered from a cylinder at broadside incidence by means of Schlieren photography. Their work has contributed significantly to our understanding of the complex interaction, at the surface of the target, between compressional waves in the fluid medium and compressional and shear waves in the solid target. Flax⁹ has shown that, because of these non-rigid impedance conditions, the responses of elastic spheres and cylinders do not approach a limiting value at high frequencies as predicted by a physical optics approximation for the scattering.

Even a casual familiarity with the work cited above suggests that there is a need for simultaneous representation of impedance effects as well as aspect and frequency dependence of a target's response. Furthermore, a formalism which relates boundary impedance, aspect dependence and frequency dependence with experimental geometry (e.g., bistatic angle) would be useful in interpreting previous and future measurements. In the author's opinion, this formalism need not be mathematically precise so long as it is illuminating, versatile and capable of numerical calculation. It is in this vein that the following work is presented.

⁸Neubauer, W. G. and Dragonette, L. R., "Observation of Waves Radiated from Circular Cylinders Caused by an Incident Pulse," J. Acoust. Soc. Am. 48, 1135-1149 (1970).

⁹Flax, L., "High ka Scattering of Elastic Cylinders and Spheres," J. Acoust. Soc. Am. 62, 1502-1503 (1977).

SECTION II

GENERAL SCATTERING THEORY

Assume that a target, whose surface, A_1 , is finite and closed, is immersed in an infinite, homogeneous, isotropic, fluid medium. An acoustic source, P, produces a compressional wave in the fluid, and a detector, D, senses acoustic waves in the medium. The source-target-detector geometry is shown in Figure 1. An arbitrary origin point, O, has been chosen, so that a representative point, S, on the target's surface is a distance \vec{r}'' from the origin. The detector, D, is located by \vec{r} from the origin point. A pseudo-origin, T, in the interior of the target is also shown.

All transmitted and reflected acoustic waves in the fluid medium are governed by the wave equation:

$$\nabla^2 \Psi(\vec{r}, t) - 1/c^2 \frac{\partial^2 \Psi(\vec{r}, t)}{\partial t^2} = -4\pi\rho(\vec{r}, t) \quad (1)$$

where $\rho(\vec{r}, t)$ is the acoustic source distribution, and $\Psi(\vec{r}, t)$ is the acoustic pressure wave. We wish to know the form of $\Psi(\vec{r}, t)$ at an observation point, \vec{r} , after including the appropriate scattering effect of the target. We may proceed to the solution by the method of Green's function. Within this approach, we may assume an impulse source and proceed to solve for the time dependence of $\Psi(\vec{r}, t)$ directly¹⁰, or we may assume a harmonic time dependence and solve for the implicit (and equivalent) frequency dependence via the Helmholtz equation (pp 803-811, Reference 10). We have selected the latter approach.

¹⁰Morse, P. M. and Feshbach, H., Methods of Theoretical Physics, McGraw-Hill Book Company, New York, pp. 834-848 (1953).

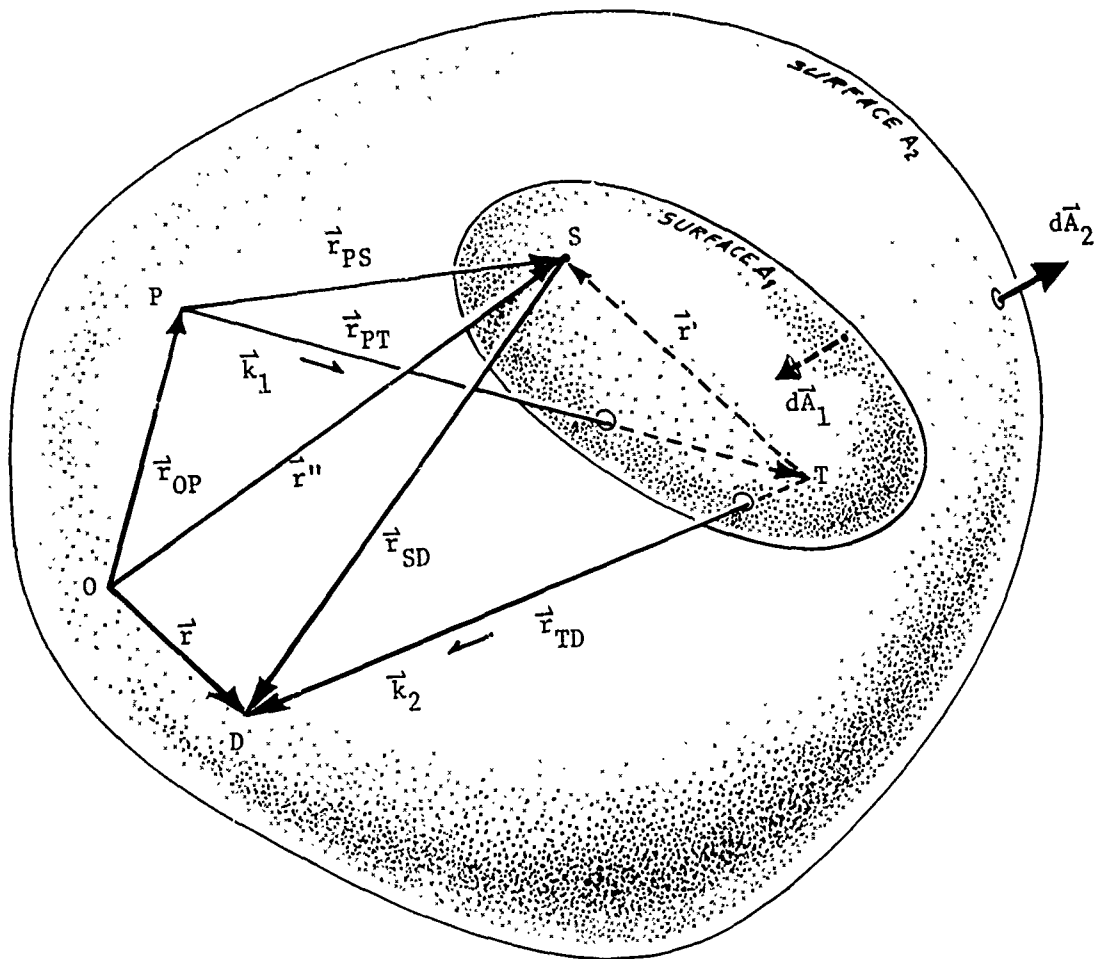


FIGURE 1. SCATTERING GEOMETRY

The time harmonic assumption is:

$$\Psi(\vec{r}, t) = \Psi(\vec{r})e^{i\omega t} \quad (2)$$

Since the scattering process is linear for infinitesimal amplitude signals, we may generate the time series for any transmitted wave shape by Fourier analysis once $\Psi(\vec{r})$ has been determined.

$$\Psi(\vec{r}, t) = \int_{-\infty}^{+\infty} T(\omega) \Psi(\vec{r})e^{i\omega t} d\omega \quad (3)$$

where $T(\omega)$ is the Fourier transform of the transmitted signal. With this option available, we now return to the wave equation.

Assume a harmonic source density for $\rho(\vec{r}, t)$ similar to equation (2). The wave equation then may be transformed from equation (1) to:

$$\nabla^2 \Psi(\vec{r}) + k^2 \Psi(\vec{r}) = -4\pi\rho(\vec{r}) \quad (4)$$

where the time dependence has been eliminated. Note that $k = \omega/c$ where "c" is the speed of the acoustic wave in the fluid medium. Equation (4) is the inhomogeneous Helmholtz equation. By definition, a Green's function satisfies the Helmholtz equation for a unit point source at a location \vec{r}'' . Thus,

$$\nabla^2 G(\vec{r}, \vec{r}'') + k^2 G(\vec{r}, \vec{r}'') = -4\pi\delta(\vec{r} - \vec{r}'') \quad (5)$$

where $\delta(\vec{r} - \vec{r}'')$ is the Dirac delta function and $G(\vec{r}, \vec{r}'')$ is the Green's function relating the field at the point \vec{r} to the source at the point \vec{r}'' .

If equation (4) is multiplied by $G(\vec{r}, \vec{r}'')$ and equation (5) is multiplied by $\Psi(\vec{r}'')$ and the difference taken, the result is:

$$\begin{aligned} G(\vec{r}, \vec{r}'') \nabla^2 \Psi(\vec{r}'') - \Psi(\vec{r}'') \nabla^2 G(\vec{r}, \vec{r}'') \\ = 4\pi [\Psi(\vec{r}'') \delta(\vec{r} - \vec{r}'') - G(\vec{r}, \vec{r}'') \rho(\vec{r}'')]. \end{aligned} \quad (6)$$

Note that the arguments in equation (4) were changed from \vec{r} to \vec{r}'' before multiplication. Equation (6) is quite general and applies for any points \vec{r} and \vec{r}'' in a common volume. We now enclose the volume containing all the source and field points of interest by two surfaces A_1 and A_2 as shown in Figure 1. Surface A_1 is the target surface while surface A_2 is at a large but arbitrary distance from all sources, targets, and field points of interest. Equation (6) may then be integrated over the volume "V" bounded by A_1 and A_2 .

$$\begin{aligned} \frac{1}{4\pi} \int_V [G(\vec{r}, \vec{r}'') \nabla^2 \Psi(\vec{r}'') - \Psi(\vec{r}'') \nabla^2 G(\vec{r}, \vec{r}'')] dV(\vec{r}'') \\ = \Psi(\vec{r}) - \int_V G(\vec{r}, \vec{r}'') \rho(\vec{r}'') dV(\vec{r}''). \end{aligned} \quad (7)$$

Note that the integral property of the Dirac delta function has been used to produce $\Psi(\vec{r})$ on the right hand side (RHS) of equation (7).

The volume integral on the left hand side (LHS) of equation (7) can be converted to a surface integral via Green's Theorem. Thus,

$$\begin{aligned} \frac{1}{4\pi} \int_{A_1} [G(\vec{r}, \vec{r}'') \vec{\nabla} \Psi(\vec{r}'') - \Psi(\vec{r}'') \vec{\nabla} G(\vec{r}, \vec{r}'')] \cdot d\vec{A}_1(\vec{r}'') \\ + \frac{1}{4\pi} \int_{A_2} [G(\vec{r}, \vec{r}'') \vec{\nabla} \Psi(\vec{r}'') - \Psi(\vec{r}'') \vec{\nabla} G(\vec{r}, \vec{r}'')] \cdot d\vec{A}_2(\vec{r}'') \\ = \Psi(\vec{r}) - \int_V G(\vec{r}, \vec{r}'') \rho(\vec{r}'') dV(\vec{r}'') \end{aligned} \quad (8)$$

where $d\vec{A}_1(\vec{r}'')$ and $d\vec{A}_2(\vec{r}'')$ are shown in Figure 1. The contribution of the surface integral over A_2 can be made vanishingly small. Various authors^{11,12} present different arguments in this regard, but none is mathematically precise. We simply shall state that the contribution from surfaces other than the target can be made vanishingly small by careful selection of the experimental conditions. When this can not be arranged, e.g., some real world operational situations, the result is a detectable contribution from A_2 known as simple reverberation. For the purposes of this description, we ignore reverberation so that equation (8) becomes:

$$\begin{aligned} \frac{1}{4\pi} \int_{A_1} [G(\vec{r}, \vec{r}'') \vec{\nabla} \Psi(\vec{r}'') - \Psi(\vec{r}'') \vec{\nabla} G(\vec{r}, \vec{r}'')] \cdot d\vec{A}_1(\vec{r}'') \\ = \Psi(\vec{r}) - \int_V G(\vec{r}, \vec{r}'') \rho(\vec{r}'') dV(\vec{r}'') \end{aligned} \quad (9)$$

The volume integral on the RHS of equation (9) can be identified by assuming the target is absent. Hence, the integral over A_1 is zero and:

$$\Psi(\vec{r}) = \int_V G(\vec{r}, \vec{r}'') \rho(\vec{r}'') dV(\vec{r}'') \quad (10)$$

The equation simply states that the wave detected at \vec{r} originates solely from the acoustic sources at \vec{r}'' . Hence, the integral on the RHS of equation (10) is the incident wave. Equation (9) may be rewritten in terms of the incident wave, $\psi_{inc}(\vec{r})$, and the scattered wave, $\psi_s(\vec{r})$ as:

$$\Psi(\vec{r}) = \psi_{inc}(\vec{r}) + \psi_s(\vec{r}) \quad (11)$$

where

$$\psi_{inc}(\vec{r}) = \int_V G(\vec{r}, \vec{r}'') \rho(\vec{r}'') dV(\vec{r}'') \quad (12)$$

¹¹Marion, J. B., Classical Electromagnetic Radiation, Academic Press, New York, 1965.

¹²Jackson, J. D., Classical Electrodynamics, John Wiley & Sons, Inc., New York, 1962.

and

$$\psi_s(\vec{r}) = \frac{1}{4\pi} \int_{A_1} [G(\vec{r}, \vec{r}'') \vec{\nabla} \psi(\vec{r}'') - \psi(\vec{r}'') \vec{\nabla} G(\vec{r}, \vec{r}'')] \cdot d\vec{A}_1(\vec{r}'') \quad (13)$$

In order to agree with the normal convention for outward pointing surface normals, the direction of $d\vec{A}_1(\vec{r}'')$ will be reversed (accompanied by the appropriate sign change) so that it points outward from the target. For purposes of simplification, the subscripts will be dropped since it will be understood henceforth that we are describing the scattered wavefield, $\psi_s(\vec{r})$, arising from the interaction of the incident wave with the target surface only. Hence,

$$\psi_s(\vec{r}) = \frac{1}{4\pi} \int_A [\psi(\vec{r}'') \vec{\nabla} G(\vec{r}, \vec{r}'') - G(\vec{r}, \vec{r}'') \vec{\nabla} \psi(\vec{r}'')] \cdot d\vec{A}(\vec{r}'') \quad (14)$$

Equation (14) is the Kirchhoff diffraction equation. It is quite general and should not be confused with the "Kirchhoff approximation" which is concerned with an approximate solution to equation (14) involving a number of assumptions.

SECTION III

EMPIRICAL SCATTERING MODEL

If the value of the wavefield and its gradient were known at each point of the target's surface, then equation (14) could be used with a spherical wave Green's function to solve for the scattered wavefield at any desired point \vec{r} . Since we do not know the value of the wavefield, let us assume that it can be represented as a linear combination of component waves; e.g., the incident wave, diffracted waves, and multiple scattered waves.

Let,

$$\Psi(\vec{r}'') = \sum_{j=1}^N \alpha_j(\vec{r}'') \psi_j(\vec{r}'') \quad (15)$$

where the $\alpha_j(\vec{r}'')$ are complex distribution functions specifying the amplitude and phase of each of the "j" components at each point on the target's surface.

Now,

$$\nabla \Psi(\vec{r}'') = \sum_{j=1}^N [\alpha_j(\vec{r}'') \vec{\nabla} \psi_j(\vec{r}'') + \psi_j(\vec{r}'') \vec{\nabla} \alpha_j(\vec{r}'')] \quad (16)$$

Substituting equations (15) and (16) into equation (14) yields:

$$\begin{aligned} \Psi(\vec{r}) = \sum_{j=1}^N \left\{ \frac{1}{4\pi} \int_A [\alpha_j(\vec{r}'') \psi_j(\vec{r}'') \vec{\nabla} G(\vec{r}, \vec{r}'') - \alpha_j(\vec{r}'') G(\vec{r}, \vec{r}'') \vec{\nabla} \psi_j(\vec{r}'') \right. \\ \left. - G(\vec{r}, \vec{r}'') \Psi(\vec{r}'') \vec{\nabla} \alpha_j(\vec{r}'')] \cdot d\vec{A}(\vec{r}'') \right\} \quad (17) \end{aligned}$$

Note, however, that each $\alpha_j(\vec{r}'')$ is a surface function, varying only parallel to the surface at any point. Hence, $\vec{\nabla}\alpha_j(\vec{r}'')$ is parallel to the surface and perpendicular everywhere to $d\vec{A}(\vec{r}'')$. Thus,

$$\vec{\nabla}\alpha_j(\vec{r}'') \cdot d\vec{A}(\vec{r}'') = 0 \quad \text{for all "j" .} \quad (18)$$

Therefore, we rewrite equation (17) as:

$$\Psi(\vec{r}) = \sum_{j=1}^N \Psi_j(\vec{r}) \quad (19)$$

where

$$\Psi_j(\vec{r}) = \frac{1}{4\pi} \int_A \alpha_j(\vec{r}'') [\Psi_j(\vec{r}'') \vec{\nabla}G(\vec{r}, \vec{r}'') - G(\vec{r}, \vec{r}'') \vec{\nabla}\Psi_j(\vec{r}'')] \cdot d\vec{A}(\vec{r}'') . \quad (20)$$

The task which remains is to postulate the nature and origin of the component waves, $\Psi_j(\vec{r}'')$, and the distribution functions, $\alpha_j(\vec{r}'')$, through physical reasoning and/or experimental measurements. As each component is added to the summation, its contribution can be compared to experimental measurements to determine its significance.

Before proceeding further, we wish to add an additional simplification. We will assume that the target is in the farfield of both the source, P, and the detector at D in Figure 1.

Now,

$$G(\vec{r}, \vec{r}'') = \frac{e^{-ik|\vec{r}-\vec{r}''|}}{|\vec{r}-\vec{r}''|} = \frac{e^{-ik|\vec{r}_{SD}|}}{|\vec{r}_{SD}|} \quad (21)$$

Using the farfield approximation and noting that $\vec{r}_{SD} = \vec{r}_{TD} - \vec{r}'$ (see Figure 1), then

$$G(\vec{r}, \vec{r}'') \stackrel{F \rightarrow F'}{\cdot} G(\vec{r}') = \left(\frac{e^{-ik_2 \cdot \vec{r}_{TD}}}{r_{TD}} \right) e^{ik_2 \cdot \vec{r}'} \quad (22)$$

where \vec{k}_2 is a wave vector parallel to \vec{r}_{TD} as shown in Figure 1. Care now must be exercised with respect to the gradient operators in equation (20). The gradient, $\vec{\nabla}G(\vec{r}, \vec{r}'')$, is with respect to \vec{r}'' while $\nabla G(\vec{r}')$ is with respect to \vec{r}' . Noting the reversal of signs of \vec{r}'' and \vec{r}' in equations (21) and (22), we see that:

$$\vec{\nabla}G(\vec{r}, \vec{r}'') = -\vec{\nabla}G(\vec{r}') \quad (23)$$

We also will assume

$$\psi_j(\vec{r}'') = \frac{e^{-ik|\vec{r}'' - \vec{r}_j|}}{|\vec{r}'' - \vec{r}_j|} = \frac{e^{-ik|\vec{r}_{jS}|}}{|\vec{r}_{jS}|} \quad (24)$$

and use the farfield approximation

$$\psi_j(\vec{r}'') \stackrel{F.F.}{\approx} \psi_j(\vec{r}') = \left(\frac{e^{-i\vec{k}_j \cdot \vec{r}_{jT}}}{r_{jT}} \right) e^{-i\vec{k}_j \cdot \vec{r}'} \quad (25)$$

where \vec{k}_j is a wave vector from the point "j" to the target origin point "T" parallel to the vector \vec{r}_{jT} . In Figure 1, this is illustrated for the incident wave from the point "P" where $\vec{k}_j = \vec{k}_1$ and $\vec{r}_{jT} = \vec{r}_{PT}$.

Noting the similarity in sign for \vec{r}'' in equation (24) and \vec{r}' in equation (25), we see that

$$\vec{\nabla}\psi_j(\vec{r}'') = \vec{\nabla}\psi_j(\vec{r}') \quad (26)$$

Now from equations (25) and (22),

$$\vec{\nabla}\psi_j(\vec{r}') = -i\vec{k}_j \psi_j(\vec{r}') \quad (27)$$

and

$$\vec{\nabla}G(\vec{r}') = i\vec{k}_2 G(\vec{r}') \quad (28)$$

Substituting equations (22), (25), (27), and (28) into equation (20) yields:

$$\psi_j(\vec{r}) = \frac{-i}{4\pi} \int_A \alpha_j(\vec{r}') \left[\frac{e^{-ik(r_{TD}+r_{jT})}}{r_{TD}r_{jT}} (\vec{k}_2 - \vec{k}_j) e^{i(\vec{k}_2 - \vec{k}_j) \cdot \vec{r}'} \right] \cdot d\vec{A}(\vec{r}'). \quad (29)$$

Let us define $\vec{k}_{2j} = \vec{k}_2 - \vec{k}_j$ and $d\vec{A}(\vec{r}') = \hat{n}dA(\vec{r}')$ where \hat{n} is an outward pointing unit normal.

Then,

$$\psi_j(\vec{r}) = \left[\frac{-i|\vec{k}_{2j}|}{4\pi} \left(e^{\frac{-ik(r_{TD}+r_{jT})}{r_{TD}r_{jT}}} \right) \right] \int_A \alpha_j(\vec{r}') \left(\frac{\vec{k}_{2j} \cdot \hat{n}}{|\vec{k}_{2j}|} \right) e^{i\vec{k}_{2j} \cdot \vec{r}'} dA(\vec{r}'). \quad (30)$$

The factor in brackets contains the experimental information regarding the distances from the incident wave source "j" to the target origin and from the target origin to the point of observation "D". The integral, on the other hand, appears characteristic of the target and its relative orientation with respect to source and detector directions.

Before examining the integral more closely, the farfield assumption merits some discussion. For sources external to the target, the farfield assumption is not very restrictive. For waves which may arise from multiple reflections in or on the target, this assumption appears invalid in principle. However, because we are at liberty to adjust the $\alpha_j(\vec{r}')$ distribution functions in amplitude and phase, we have sacrificed no generality in principle. We have made no real assumption and hence produced no apparent simplification. The simplification is in form only as manifested by the form of the integral in equation (30).

Let us define

$$F_A(\vec{k}_{2j}) = \int_A \left\{ \alpha_j(\vec{r}') \left(\frac{\vec{k}_{2j} \cdot \hat{n}}{|\vec{k}_{2j}|} \right) \right\} e^{i\vec{k}_{2j} \cdot \vec{r}'} dA(\vec{r}') \quad (31)$$

where $F_A(\vec{k}_{2j})$ is the structure factor of target "A". Note that the structure factor and the factor inside the braces of the integral are a Fourier transform pair. The factor in braces may be called the "j"th component of the target characteristic function. Because of the Fourier relationship, we may construct a wave space for $F_A(\vec{k}_{2j})$ which is conjugate to the real space which is the domain of the characteristic function. This concept originated over 50 years ago in x-ray diffraction^{13,14} and has been discussed more recently by Lewis¹⁵ in connection with physical optics inverse diffraction. The Ewald construction, which relates the incident wave vector $\vec{k}_j = \vec{k}_1$ and the scattered wave vector \vec{k}_2 to the argument \vec{k}_{21} of $F_A(\vec{k}_{21})$, has been discussed briefly¹⁶ but will be included for completeness in the description of wave space in the next section.

¹³Ewald, P. P., "Zur Theorie der Interferenzen der Rontgenstrahlen in Kristallen," Physik. Z. 14, 465 (1913).

¹⁴Pepinsky, R. and Vand, V., "Crystallography and X-Ray Diffraction," Handbook of Physics, E. V. Condon and H. Odishaw (eds.), McGraw-Hill Book Company, Inc., New York, pp. 8-1 to 8-23 (1958).

¹⁵Lewis, R. M., "Physical Optics Inverse Diffraction," IEEE Transactions on Antennas and Propagation 17, 308-314 (1969).

¹⁶Nelander, J. C., "Modeling Acoustic Scattering from Elastic Cylinders," NCSC Technical Note 477, March 1977.

SECTION IV

REAL SPACE - WAVE SPACE RELATIONSHIPS

BASIS VECTORS

In order to simplify the discussion which follows, let us consider the case for $j = 1$ and drop the subscripts and superscripts from equation (31). Thus,

$$F(\vec{k}) = \int [\alpha(\vec{r}) \frac{\vec{k} \cdot \hat{n}}{|\vec{k}|}] e^{i\vec{k} \cdot \vec{r}} dA(\vec{r}) \quad (32)$$

where $\vec{k} = \vec{k}_{21} = \vec{k}_2 - \vec{k}_1$.

A real space coordinate system may be defined with basis vectors \vec{a}_1 , \vec{a}_2 and \vec{a}_3 so that:

$$\vec{r} = x\vec{a}_1 + y\vec{a}_2 + z\vec{a}_3 \quad (33)$$

A wave space coordinate system, conjugate to the real space system, may be constructed using the following relations:

$$\vec{b}_\ell = \frac{\vec{a}_m \times \vec{a}_n}{\vec{a}_\ell \cdot \vec{a}_m \times \vec{a}_n} \quad (34)$$

and

$$\vec{a}_\ell \cdot \vec{b}_m = \delta_{\ell m} \quad (35)$$

where $\ell, m, n = 1, 2, 3$ in cyclic combination and $\delta_{\ell m}$ is the Kronecker delta. Thus,

$$\vec{k} = k_x \vec{b}_2 + k_y \vec{b}_2 + k_z \vec{b}_3 \quad (36)$$

and

$$\vec{k} \cdot \vec{r} = k_x x + k_y y + k_z z \quad (37)$$

The basis vectors in either wave or real space need not be orthonormal¹⁴ and usually are not when symmetry conditions are more important than the simplification produced by orthonormality. For our purposes, we shall assume orthonormality.

The conjugate relationship between a real space characteristic function and a wave space structure factor is illustrated in Figure 2. The Fourier relationship between the two, equation (32), ensures that complete knowledge of one is equivalent to complete knowledge of the other. Equation (30) indicates that we can gain knowledge about the structure factor (and, hence, the target characteristic function) by

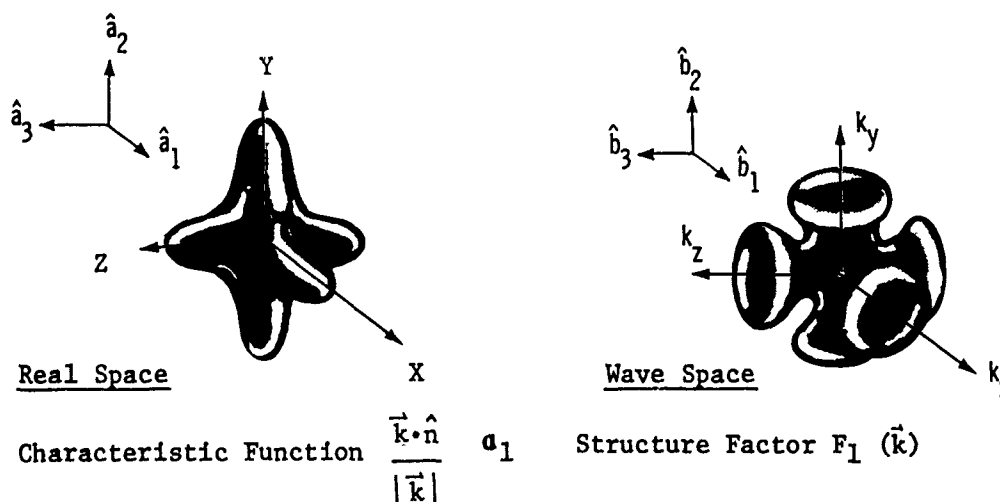


FIGURE 2. REAL SPACE - WAVE SPACE RELATIONSHIP

¹⁴ibid

measuring the acoustic wavefield scattered by a target. Several important points warrant further discussion. For example: (1) how is the characteristic function related to such familiar target parameters as shape, size, and orientation? (2) what parts of the structure factor can be measured in a given source-target-detector geometry utilizing a specific transmitted waveform? (3) is the structure factor, and hence target characteristic function, unique; i.e., independent of source-target-detector geometry? (4) is there a minimal set of measurements which can be made which will identify a given class of targets with a high probability of success? The answer to the fourth question can be attempted only after completing a modeling and measurement effort. Information which will be useful in answering the other questions is provided here.

EWALD CONSTRUCTION

The Ewald construction¹³ can be used to relate experimental parameters to the range of $F(\vec{k})$ values which are observable by that experiment. Assume that the incident plane wave is in the direction \vec{k}_1 . In wave space, a sphere of radius $|\vec{k}_1| = 2\pi/\lambda$ can be drawn such that its diameter, along the \vec{k}_1 direction, passes through the origin of wave space coordinates so that the sphere is tangent to the origin. The scattered wave vector, \vec{k}_2 , is drawn from the center of this sphere in the scattered wave direction. The resulting construction is shown in Figure 3(A). Note that the vector $\vec{k} = \vec{k}_2 - \vec{k}_1$ has its terminus on the sphere regardless of the direction of \vec{k}_2 . Hence, for a given target orientation with respect to \vec{k}_1 , only those values of $F(\vec{k})$ lying on the surface of the sphere are observable regardless of the position of the detector. If a transmitted signal has a finite bandwidth (rather than monochromatic), then two spheres with radii $|\vec{k}_1|(\max)$ and $|\vec{k}_1|(\min)$ may be drawn as shown in Figure 3(B). The high frequency limit of the incident wave, $|\vec{k}_1|(\max)$, defines the larger sphere while the low frequency limit, $|\vec{k}_1|(\min)$, specifies the smaller

¹³ibid

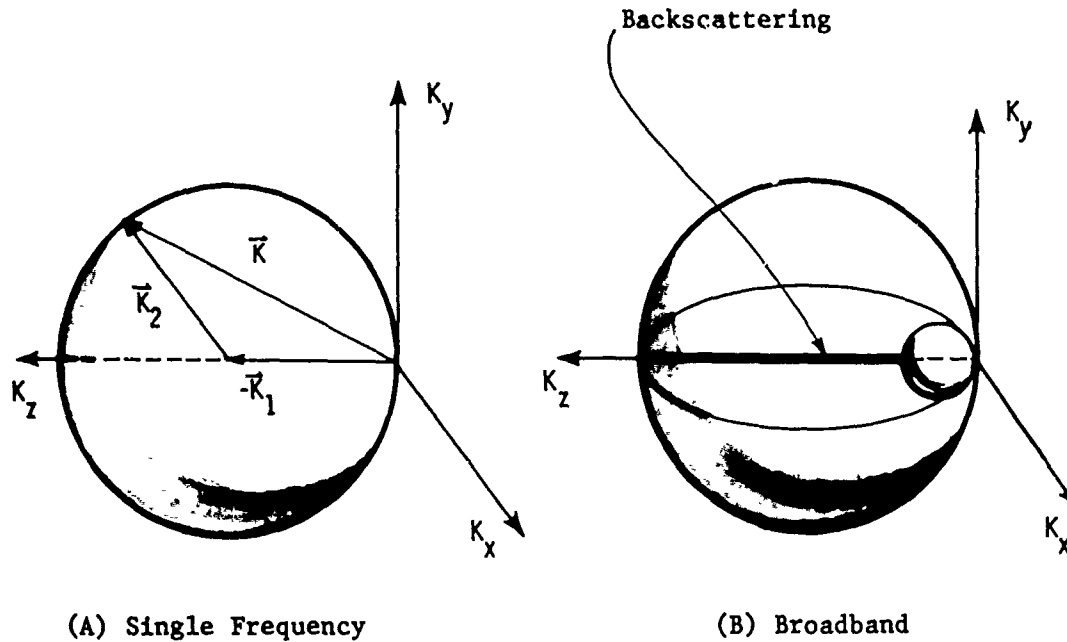


FIGURE 3. EWALD CONSTRUCTION

sphere. Observable values of $F(\vec{k})$ are contained in the volume inside the larger sphere but outside the smaller sphere. The line of $F(\vec{k})$ values which can be observed with a broadband incident wave and a backscattering configuration, i.e., $\vec{k}_2 = -\vec{k}_1$, is shown in Figure 3(B). With the help of Figure 3(B) and a little imagination, one can see that the same $F(\vec{k})$ value can be observed by more than one experimental configuration. But these values will occur for different frequencies. It should be emphasized that these would be the same $F(\vec{k})$ values, not just equal $F(\vec{k})$ values. This occurs because of the multitude of ways that the same vector \vec{k} can be constructed from different \vec{k}_1 and \vec{k}_2 vectors. Note that $\vec{k} = \vec{k}_2 - \vec{k}_1$, and that \vec{k} , not \vec{k}_1 , determines the frequency at which the $F(\vec{k})$ value will be observed.

Although the above relationships are literally true for diffraction where equation (32) represents the total structure factor, the relationships for acoustic scattering, where multiple-scattered waves may be of considerable significance, are bound to be more complex. Suffice it to say that caution should be exercised when comparing backscattering measurements to bistatic measurements for the same target. Some polar plots, such as those by Barnard and McKinney¹, which display the scattering cross section, $|\vec{k}|^2 \cdot |F(\vec{k})|^2$, where the projector and target are stationary while the detector is moved in a circle around the target, are variable bistatic angle measurements. The $F(\vec{k})$ values so measured would fall on a circle on the surface of a single sphere such as that shown in Figure 3A. If the same target were examined by backscattering measurements, using the same frequency, the series of $F(\vec{k})$ values so measured would trace out a circle of radius $2|\vec{k}_1|$ whose center is the origin of the wave space coordinate system rather than the center of the Ewald sphere in Figure 3(A). Whether or not there exists an operator such that:

$$R_{op} [F(\vec{k})_{\text{bistatic}}] = F(\vec{k}')_{\text{backscattering}} \quad (38)$$

for acoustic scattering is not known. It is the author's opinion that a thorough understanding of R_{op} is equivalent to a thorough understanding of acoustic scattering.

INCLINATION FACTOR

One final point is worth amplification. The factor,

$$\frac{\vec{k} \cdot \hat{n}}{|\vec{k}|}$$

in equation (32) is simply a variant of the Stokes inclination factor of physical optics. Consider the reflection of an incident wave \vec{k}_1 from a

planar surface, whose unit normal is \hat{n} , into the specular direction \vec{k}_s as shown in Figure 4. Since $\vec{k}_1 = \vec{k}_s$ and $\theta_1 = \theta_s$, it is easy to see that $\vec{k} = \vec{k}_s - \vec{k}_1$ is parallel to \hat{n} and hence the inclination factor is maximum; i.e.,

$$\frac{\vec{k} \cdot \hat{n}}{|\vec{k}|} = 1 . \quad (39)$$

For directions other than specular, i.e., $\vec{k}_2 \neq \vec{k}_s$, the inclination factor specifies the appropriate weight for the reflectivity of that point into the direction specified by \vec{k}_2 . The inclination factor is non-negative and is minimum when \vec{k}_1 is parallel to the surface and \vec{k}_2 is parallel or anti-parallel to \vec{k}_1 . When applying the inclination factor, one need not be concerned with deviations from the specular direction but only with the relationship between \vec{k} and \hat{n} .

(Text Continued on Page 22)

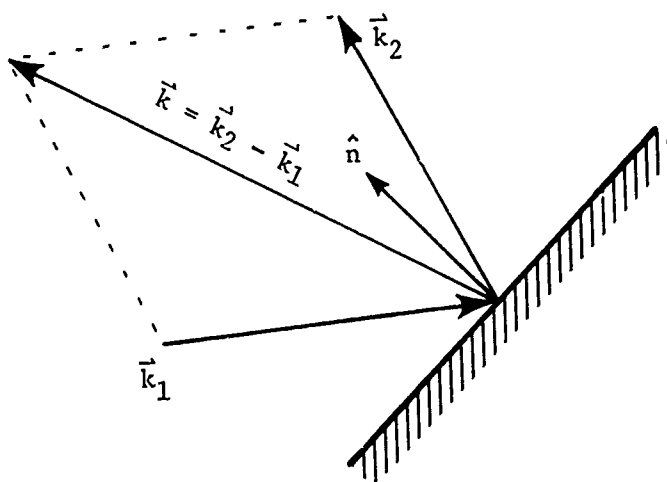
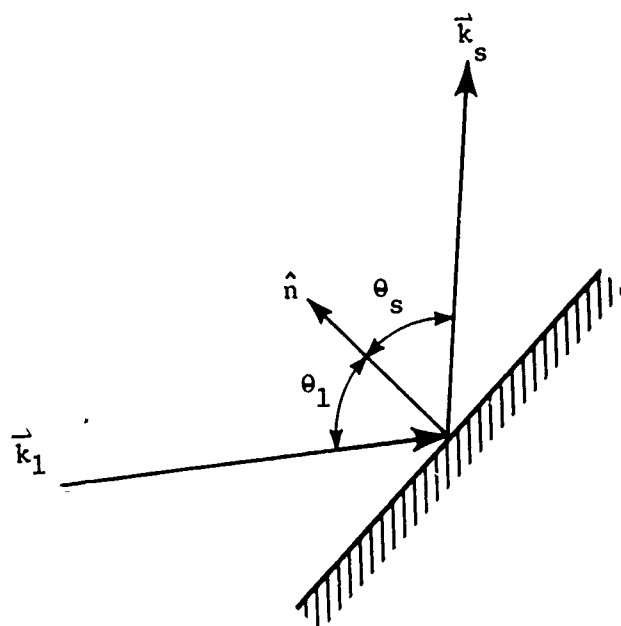


FIGURE 4. INCLINATION FACTOR $\left(\frac{\vec{k} \cdot \hat{n}}{|\vec{k}|} \right)$ RELATIONSHIPS

SECTION V

RIGID CYLINDER SCATTERING - FIRST LEVEL APPROXIMATION

GENERAL APPROACH

In order to illustrate the utility of the empirical model derived in Section III, let us consider scattering from a rigid, finite cylinder at an arbitrary orientation or aspect angle. Objects with edges, such as the finite cylinder, pose particularly difficult problems in scattering theory because: (1) the edges produce multiple scattering effects, and (2) the edges are the loci of discontinuities in geometry and hence make integration of wavefields across these areas difficult.

A simple scattering model by Freedman¹⁷ cites these discontinuities as the principle source of scattering. Freedman's image point model of acoustic scattering is a scalar model in which the target's surface is viewed from a common source-detector position (backscattering). Dunsiger⁷ has noted that the integral of the image point model is difficult to evaluate because of discontinuities in the integrand. These discontinuities are the image points. Although the structure factor for our empirical model given in equation (31) is similar to Freedman's integral, a judicious choice of integration procedure can avoid mathematical difficulties. Note also that equation (31) is a vector rather than scalar representation. The integration now will be illustrated for the rigid, right circular cylinder shown in Figure 5.

The radius of the cylinder is "a," and its length is "L." The cylinder axis is aligned parallel to the real space z-axis. We divide the surface of the cylinder into two parts: S_1 , the end disc, and S_2 ,

¹⁷Freedman, A., "A Mechanism of Acoustic Echo Formation," Acustica 12, 10-21 (1962).

⁷ibid

(Text Continued on Page 24)

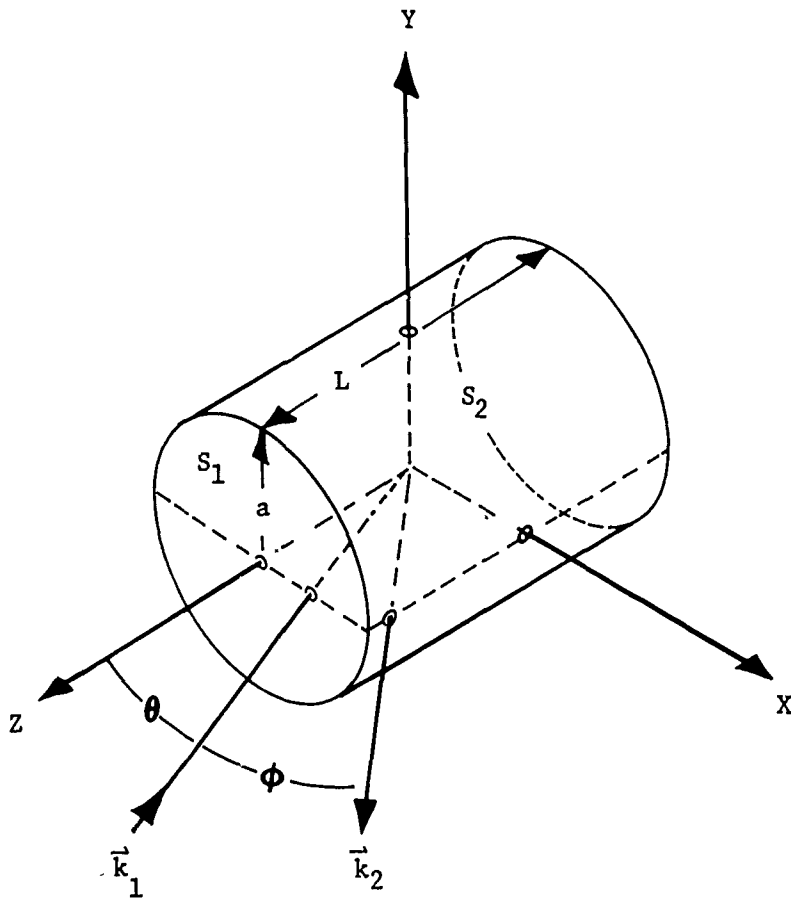


FIGURE 5. GEOMETRY FOR SCATTERING FROM A RIGID, RIGHT CIRCULAR CYLINDER

the curved surface. We will consider only the first level approximation; i.e., only the incident wave from the source is considered and all body-diffracted and multiple-scattered waves are ignored.

The structure factor is:

$$F(\vec{k}) = \int \alpha(\vec{r}) \frac{[\vec{k} \cdot \hat{n}]}{|\vec{k}|} e^{i\vec{k} \cdot \vec{r}} dA(\vec{r}) \quad (40)$$

The distribution function is:

$$\alpha(\vec{r}) = \sum_{m=1}^M \theta[-\vec{k}_1 \cdot \hat{n}_m] \theta[\vec{k}_2 \cdot \hat{n}_m] \quad (41)$$

where $\theta(x) = 1, x > 0; \theta(x) = 0, x \leq 0$ (42)

and "m" denotes the various analytic surfaces of the target. Hence, equation (41) states that only those surfaces observable from both the source and detector are of significance. We may confine our investigation to the x-z quadrant of Figure 5, because of symmetry. Further, we require \vec{k}_2 to be coplanar with \vec{k}_1 and the cylinder axis. This imposes some restriction on the generality of our solution. Equation (41) is nonzero for S_1 and one half the curved side surface (S_2) of the cylinder. We may write:

$$F(\vec{k}) = F_{S_1}(\vec{k}) + F_{S_2}(\vec{k}) \quad (43)$$

where F_{S_1} and F_{S_2} are the structure factors of the end disc and hemi-cylinder respectively. Each structure factor may be evaluated separately and summed to produce the total $F(\vec{k})$.

CYLINDER END DISC STRUCTURE FACTOR

For the end disc:

$$F_{S_1}(\vec{k}) = \int_{S_1} \frac{\vec{k} \cdot \hat{n}}{|\vec{k}|} e^{i\vec{k} \cdot \vec{r}} dA_1(\vec{r}). \quad (43)$$

Now from Figure 6, we see that:

$$\vec{r} = \frac{L}{2} \hat{z} + \vec{x} \quad (44)$$

and, $dA(\vec{r}) = 2ydx = 2(a^2-x^2)^{\frac{1}{2}} dx$. (45)

Thus,

$$F_{S_1}(\vec{k}) = \int_z \int_{-a}^{+a} \delta(z-\frac{L}{2}) 2(a^2-x^2)^{\frac{1}{2}} \frac{\vec{k} \cdot \hat{n}}{|\vec{k}|} e^{i(k_x x + k_z z)} dx dz. \quad (46)$$

Note, from Figure 5, $\vec{k} \cdot \hat{n} = \vec{k} \cdot \hat{z} = k_z$ for the surface S_1 .

Thus equation (46) can be integrated over dz and simplified to:

$$F(\vec{k})_{S_1} = \frac{2k_z}{|\vec{k}|} e^{i\frac{k_z L}{2}} \int_{-a}^{+a} (a^2-x^2)^{\frac{1}{2}} e^{ik_x x} dx. \quad (47)$$

The integral in equation (47) can be simplified as shown below.

$$\int_{-a}^{+a} (a^2-x^2)^{\frac{1}{2}} e^{ik_x x} dx = 2 \int_0^a (a^2-x^2)^{\frac{1}{2}} \cos(k_x x) dx. \quad (48)$$

Let, $t = \frac{x}{a}$; $dt = \frac{dx}{a}$; $x=0 \rightarrow t=0$; $x=a \rightarrow t=1$.

Thus the integral becomes:

$$2a^2 \int_0^1 (1-t^2)^{\frac{1}{2}} \cos[(k_x a)t] dt. \quad (49)$$

The integral (49) is a form of the first order Bessel function.¹⁸

Thus,

¹⁸Abramowitz, M. and Stegun, I. A., Handbook of Mathematical Functions, Dover Publication, Inc., New York, 1965.

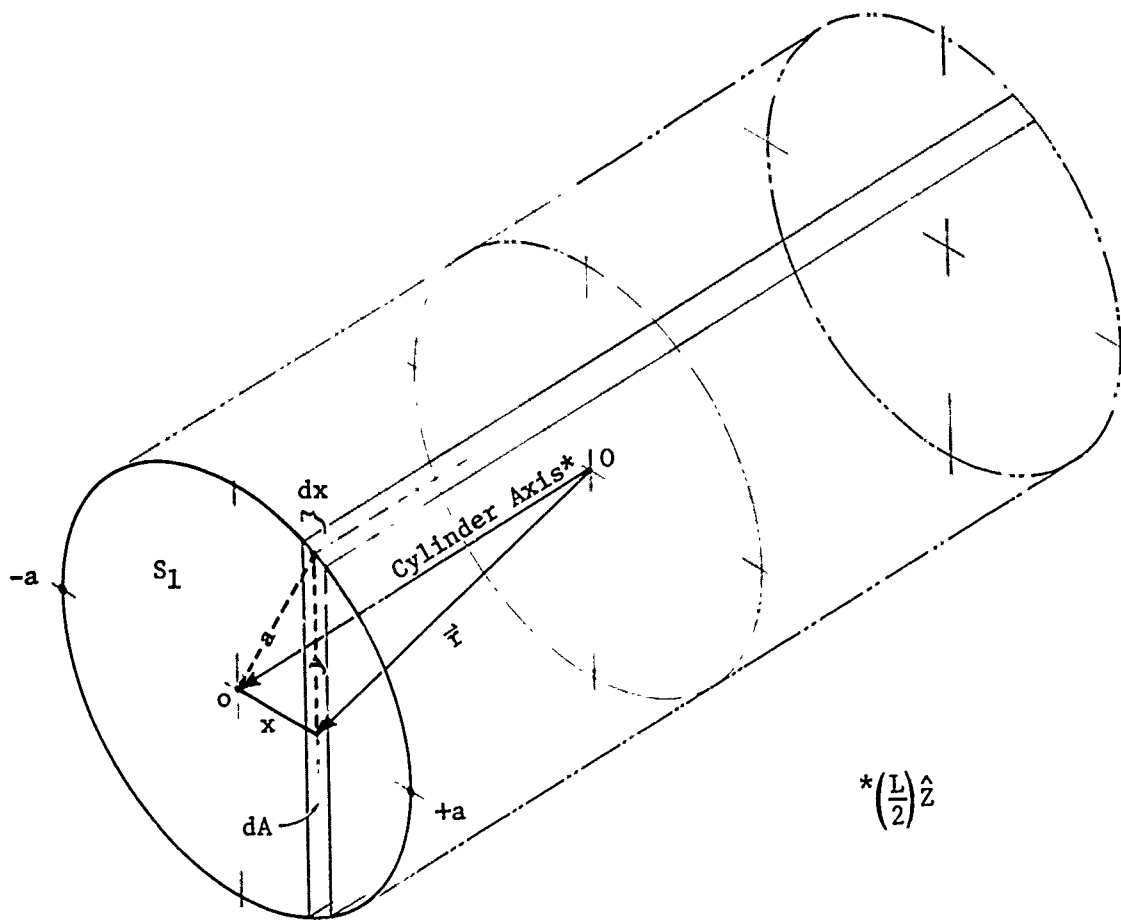


FIGURE 6. CYLINDER END DISC (S_1)

$$F_{S_1}(\vec{k}) = (2\pi a^2 e^{ik_z L/2}) \frac{k_z}{|\vec{k}|} \left[\frac{J_1(k_x a)}{k_x a} \right]$$

where $J_1(k_x a)$ is a first-order Bessel function,

$$J_1(z) = (\frac{1}{2}z) \sum_{n=0}^{\infty} \frac{(-\frac{1}{4}z^2)^n}{n! \Gamma(n+2)}$$

and " Γ " is the gamma function.

CYLINDER SIDE SURFACE STRUCTURE FACTOR

In order to evaluate the structure factor for the hemi-cylinder, consider the diagram in Figure 7. Note that $\vec{r} = \vec{\rho} + \vec{z}$ and $\vec{\rho} = \vec{x} + \vec{y}$. Now the unit normal to the surface is:

$$\hat{n} = \frac{\vec{\rho}}{a} = \frac{\vec{x} + \vec{y}}{a}$$

Thus,

$$\frac{\vec{k} \cdot \hat{n}}{|\vec{k}|} = \frac{\vec{k} \cdot \vec{x} + \vec{k} \cdot \vec{y}}{|\vec{k}|} = \frac{k_x x}{|\vec{k}|} \tag{51}$$

since $\vec{k} \cdot \vec{y} = 0$ because \vec{k} lies in the x-z plane (see above). The differential area element in Figure 7 can be written as:

$$dA = a d\phi dz$$

$$= -\frac{a dx dz}{(a^2 - x^2)^{\frac{1}{2}}} \quad (\text{for } a > x > 0) \tag{52a}$$

$$\text{or} \quad = +\frac{a dx dz}{(a^2 - x^2)^{\frac{1}{2}}} \quad (\text{for } 0 < x < a) \tag{52b}$$

The two forms of equation (52) are needed for the positive and negative values of "y." Thus, we may write:

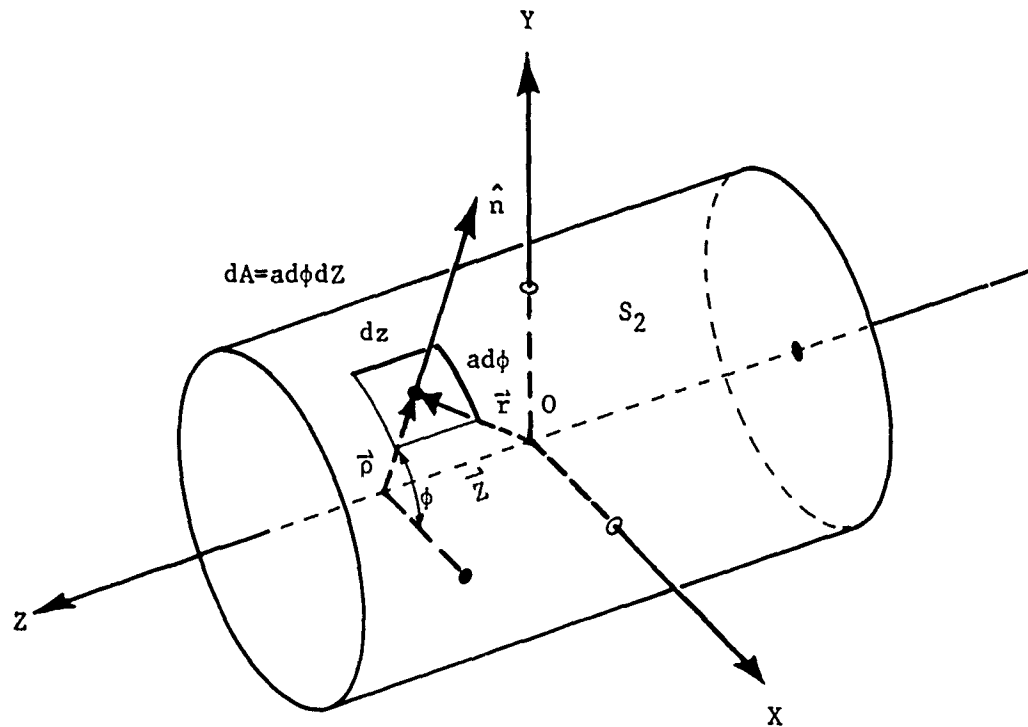


FIGURE 7. CYLINDER SIDE SURFACE (S_2)

$$\begin{aligned}
 F_{S_2}(\vec{k}) &= \int_{S_2} \frac{\vec{k} \cdot \hat{n}}{|\vec{k}|} e^{i\vec{k} \cdot \vec{r}} dA(\vec{r}) \\
 &= \int_{-L/2}^{+L/2} e^{ik_z z} dz \left[\int_0^a dx \left(\frac{k_x x}{|\vec{k}| a} \right) \frac{ae^{ik_x x}}{(a^2 - x^2)^{1/2}} \right. \\
 &\quad \left. - \int_a^0 dx \left(\frac{k_x x}{|\vec{k}| a} \right) \frac{ae^{ik_x x}}{(a^2 - x^2)^{1/2}} \right] \\
 &= \frac{2k_x}{|\vec{k}|} \int_{-L/2}^{+L/2} e^{ik_z z} dz \left[\int_0^a \frac{xe^{ik_x x}}{(a^2 - x^2)^{1/2}} dx \right] \tag{53}
 \end{aligned}$$

Now,

$$\int_{-L/2}^{+L/2} e^{ik_z z} dz = \frac{e^{ik_z L/2} - e^{-ik_z L/2}}{ik_z}$$

$$= L \left[\frac{\sin\left(\frac{k_z L}{2}\right)}{\frac{k_z L}{2}} \right] \quad (54)$$

Thus,

$$F_{S_2}(\vec{k}) = \frac{2k_x L}{|\vec{k}|} \left[\frac{\sin\left(\frac{k_z L}{2}\right)}{\left(\frac{k_z L}{2}\right)} \right] \left[\int_0^a \frac{x e^{ik_x x}}{(a^2 - x^2)^{1/2}} dx \right] \quad (55)$$

To evaluate the integral remaining in equation (55) we make the substitutions,

$$t = \frac{x}{a}; \quad dt = \frac{dx}{a}; \quad x = 0 \rightarrow t = 0; \quad x = a \rightarrow t = 1.$$

Therefore,

$$\int_0^a \frac{x e^{ik_x x}}{(a^2 - x^2)^{1/2}} dx = a \int_0^1 \frac{t e^{i(k_x a)t}}{(1-t^2)^{1/2}} dt \quad (56)$$

We now integrate by parts using the following identifications:

$$u = e^{i(k_x a)t}; \quad du = i(k_x a) e^{i(k_x a)t} dt \quad (57a)$$

$$dv = \frac{tdt}{(1-t^2)^{1/2}}; \quad v = -(1-t^2)^{-1/2} \quad (57b)$$

Thus,

$$\int_0^1 \frac{t e^{ik_x at}}{(1-t^2)^{1/2}} dt = -(1-t^2)^{-1/2} e^{ik_x at} \Big|_0^1 + i(k_x a) \int_0^1 (1-t^2)^{-1/2} e^{ik_x at} dt$$

$$= 1 + ik_x a \int_0^1 (1-t^2)^{\frac{1}{2}} e^{ik_x at} dt. \quad (58)$$

In order to identify the integral in equation (58), we write it in the following form:

$$\begin{aligned} \int_0^1 (1-t^2)^{\frac{1}{2}} e^{ik_x at} dt &= \int_0^1 (1-t^2)^{\frac{1}{2}} \cos[(k_x a)t] dt \\ &+ i \int_0^1 (1-t^2)^{\frac{1}{2}} \sin [(k_x a)t] dt . \end{aligned} \quad (59)$$

The first integral on the RHS of equation (59) is a form of the first-order Bessel function¹⁸ (see also equation (49)) while the second integral on the RHS of equation (59) is a form of the first-order Struve function¹⁸, $H_1(z)$, where:

$$H_1(z) = (\frac{1}{2}z)^2 \sum_{n=0}^{\infty} \frac{(-1)^n (\frac{1}{2}z)^{2n}}{\Gamma(n+3/2) \Gamma(n+5/2)} \quad (60)$$

where Γ is the gamma function.

Equation (58) now can be put in the form:

$$\begin{aligned} \int_0^1 \frac{te^{ik_x at}}{(1-t^2)^{\frac{1}{2}}} dt &= 1 - k_x a \left(\frac{\pi^{\frac{1}{2}} \Gamma(3/2)}{k_x a} \right) H_1(k_x a) + ik_x a \left(\frac{\pi^{\frac{1}{2}} \Gamma(3/2)}{k_x a} \right) J_1(k_x a) \\ &= [1 - \frac{\pi}{2} H_1(k_x a)] + i [\frac{\pi}{2} J_1(k_x a)] \end{aligned} \quad (61)$$

Using equations (56) and (61) in equation (55) we find:

$$F_{S_2}(\vec{k}) = \pi a L \left(\frac{k_x}{|\vec{k}|} \right) \left[\frac{\sin(\frac{k_z L}{2})}{(\frac{k_z L}{2})} \right] \left[\left(\frac{2}{\pi} - H_1(k_x a) \right) + i J_1(k_x a) \right] \quad (62)$$

¹⁸ibid

COMBINED STRUCTURE FACTOR

In order to combine $F_{S_1}(\vec{k})$ with $F_{S_2}(\vec{k})$, we rewrite the exponential factor in equation (50),

$$e^{i\frac{k_z L}{2}} = \cos\left(\frac{k_z L}{2}\right) + i \sin\left(\frac{k_z L}{2}\right). \quad (63)$$

Equation (50) then becomes:

$$F_{S_1}(\vec{k}) = 2\pi a^2 \frac{k_z}{|\vec{k}|} \left[\frac{J_1(k_x a)}{(k_x a)} \right] \left[\cos\left(\frac{k_z L}{2}\right) + i \sin\left(\frac{k_z L}{2}\right) \right] \quad (64)$$

Combining equations (62) and (64) yields:

$$\begin{aligned} F(\vec{k}) &= F_{S_1}(\vec{k}) + F_{S_2}(\vec{k}) \\ &= \left\{ \frac{2\pi a^2 k_z}{|\vec{k}| k_x a} \cos\left(\frac{k_z L}{2}\right) J_1(k_x a) + \frac{2\pi a L k_x}{|\vec{k}| k_z L} \sin\left(\frac{k_z L}{2}\right) \left[\frac{2}{\pi} - H_1(k_x a) \right] \right\} \\ &\quad + i \left\{ \frac{2\pi a^2 k_z}{|\vec{k}| k_x a} \sin\left(\frac{k_z L}{2}\right) J_1(k_x a) + \frac{2\pi a L k_x}{|\vec{k}| k_z L} \sin\left(\frac{k_z L}{2}\right) J_1(k_x a) \right\}. \quad (65) \end{aligned}$$

Thus, the total structure factor, to this first level approximation, for the rigid, right circular cylinder is:

$$\begin{aligned} F(\vec{k}) &= \frac{2\pi a}{|\vec{k}|} \left\{ \frac{k_z}{k_x} \cos\left(\frac{k_z L}{2}\right) J_1(k_x a) + \frac{k_x}{k_z} \sin\left(\frac{k_z L}{2}\right) \left[\frac{2}{\pi} - H_1(k_x a) \right] \right\} \\ &\quad + i \left\{ \left(\frac{k_z}{k_x} + \frac{k_x}{k_z} \right) \sin\left(\frac{k_z L}{2}\right) J_1(k_x a) \right\} \quad (66) \end{aligned}$$

where $J_1(k_x a)$ is first-order Bessel function and $H_1(k_x a)$ is a first-order Struve function defined in series form by equations (50a) and (60), respectively.

SECTION VI

RIGID CYLINDER SCATTERING CROSS SECTION

The structure factor, equation (66), is valid for both bistatic scattering and backscattering, to the level of approximation indicated by equations (41) and (42), as long as \vec{k}_1 , \vec{k}_2 , and the cylinder axis are coplanar. The nature of the structure factor can be examined by plotting the dimensionless scattering cross-section, Ω :

$$\Omega(\zeta) = [\zeta \cdot F(\zeta)]^2 \quad (67)$$

where $\zeta = |\vec{k}|a$. The dimensionless parameter ζ is proportional to the ratio of the nominal target dimension (in this case, the cylinder radius "a") to the wavelength of the acoustic waves used to provide the scattering information. Hence, a particular value of $\Omega(\zeta)$ is representative of a large target at low frequency or a small target at high frequency when similar scaling factors are applied to the target dimension and wavelength.

A three-dimensional plot in wave space of the scattering cross-section for a rigid cylinder whose radius to length ratio is 6 is shown in Figure 8. The ordinate in Figure 8, $\Omega(\zeta)$, is measured in decibels relative to the maximum value in the plot. The ζ_z axis corresponds to the end-on aspect of the cylinder while the ζ_x axis is the broadside response. Only one quadrant of the function $\Omega(\zeta)$ is shown since the others are similar by reason of symmetry. A shaded contour plot of $\Omega(\zeta)$ showing all four quadrants is shown in Figure 9. Generally speaking, the darker the region in Figure 9, the larger the $\Omega(\zeta)$ value. However, caution should be exercised when interpreting Figure 9 since it is a black and white reproduction of a color-coded display.

(Text Continued on Page 35)

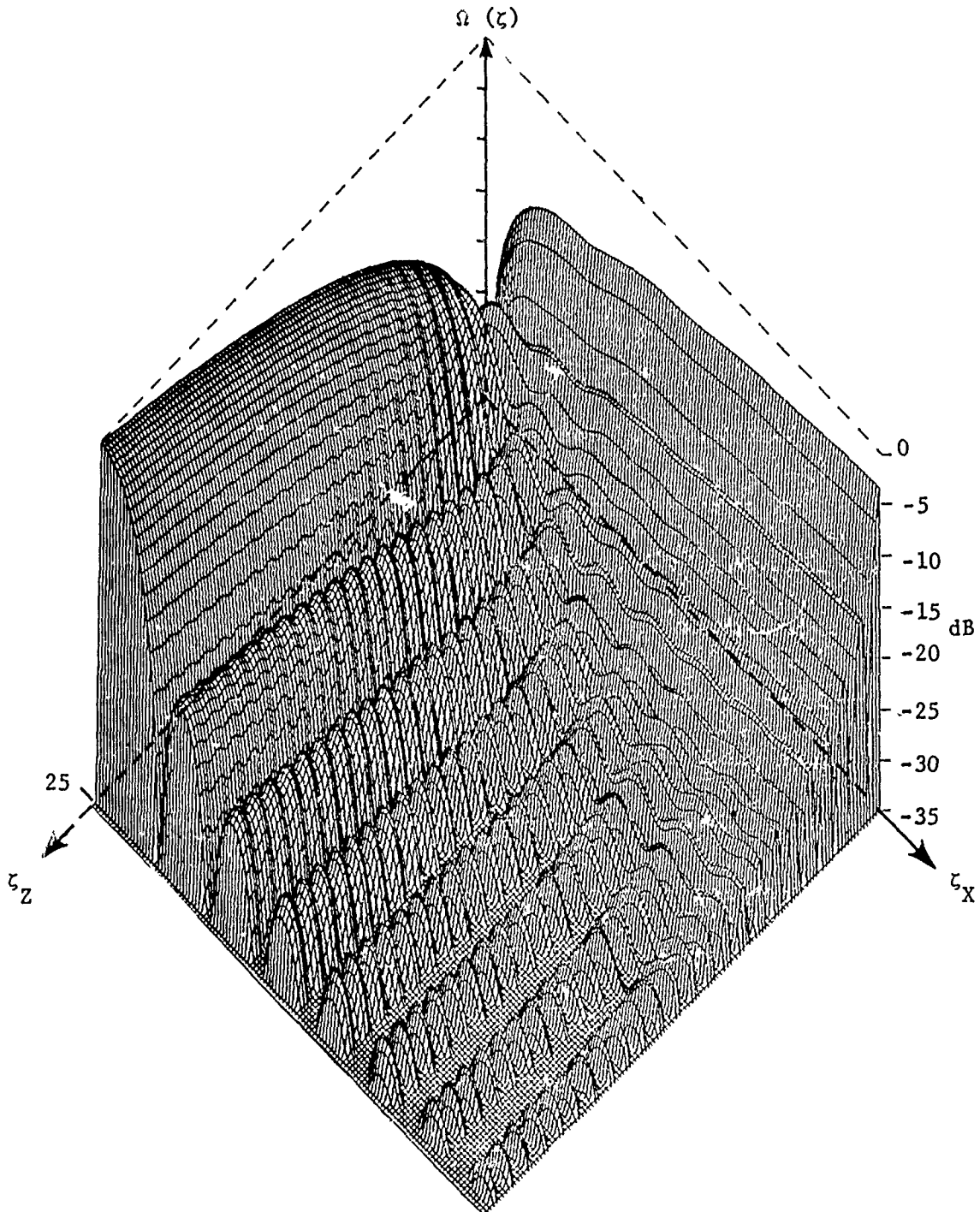


FIGURE 8. RIGID CYLINDER SCATTERING CROSS-SECTION

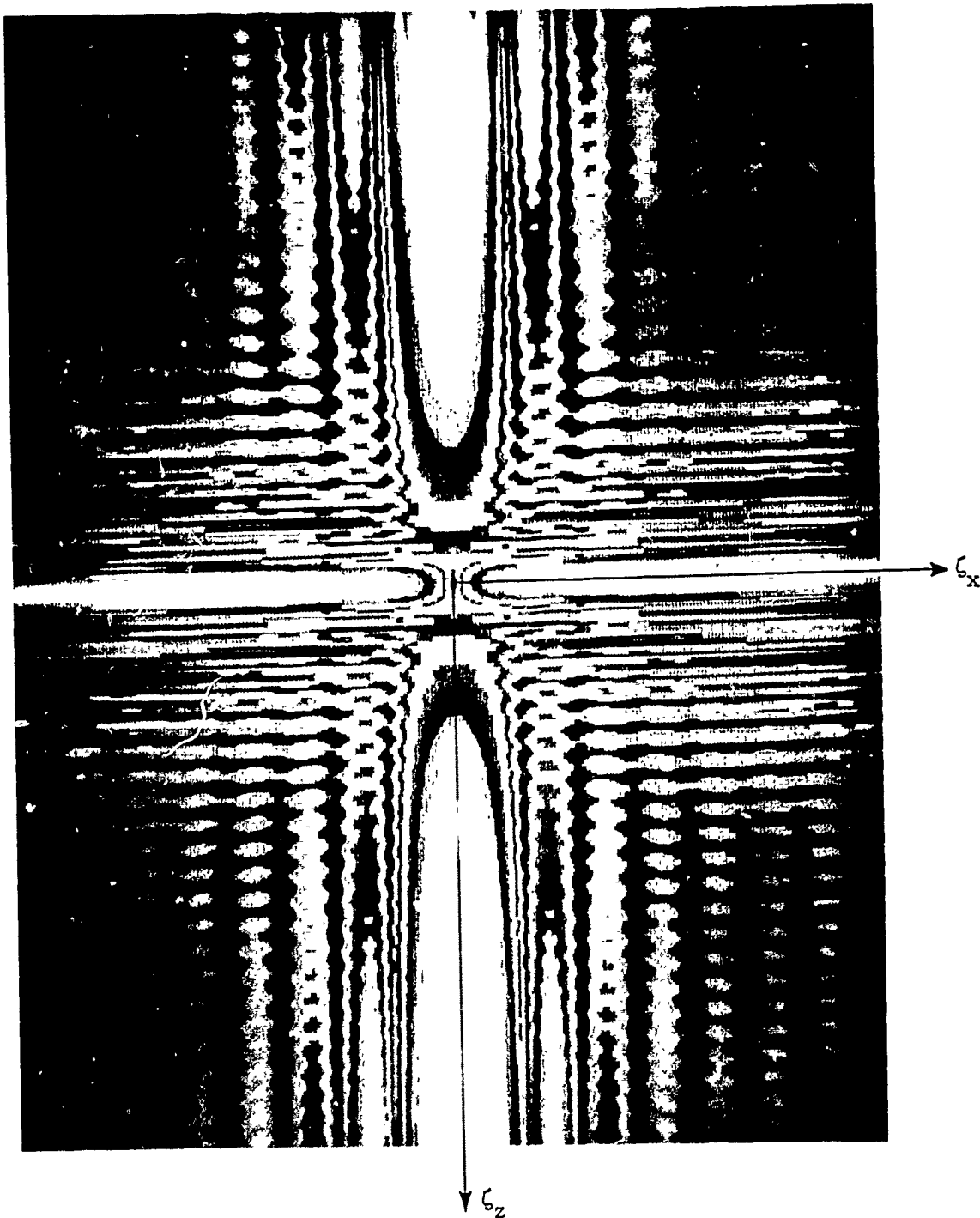


FIGURE 9. SHADED CONTOUR PLOT SHOWING THE FOUR QUADRANTS OF THE RIGID CYLINDER SCATTERING CROSS-SECTION

When interpreting either Figure 8 or Figure 9, one should imagine that the target is located at the origin of coordinates of each plot with the cylinder axis oriented along the ζ_z axis. The response which would be observed in a given backscattering situation can be found by drawing a radial line from the origin of the plot in the direction corresponding to the target viewing or aspect angle. The appropriate response is located on this line at a distance from the origin corresponding to 4π times the ratio of the radius "a" to the wavelength " λ ." Thus, the responses for higher frequencies are located at larger radial distances from the origin. The maximum values of $\zeta = 4\pi(a/\lambda)$ shown in Figures 8 and 9 is 25.

A few comments on the interpretation of Figure 8 are worthwhile. First, the scattering cross-section increases monotonically with frequency for constant values of the structure factor, $F(\zeta)$. In a linear plot, this increase would be quadratic. It arises because of the factor ζ^2 in $\Omega(\zeta)$. This increase can be seen along the ζ_z axis of Figure 8 where $F(\zeta)$ is constant. The ζ^2 factor is a part of the definition of scattering cross-section since $\Omega(\zeta)$ conventionally is defined in terms of energy scattered into a given solid angle. In order to compensate for the spherical spreading of the energy of a scattered wavefield (remember, since $\Psi(\vec{r})$ is proportional to $F(\vec{k})$, or in terms of our dimensionless parameter $F(\zeta)$, the energy density $F^2(\zeta)$ must be multiplied by a factor proportional to the area of a sphere in wavespace, i.e., the radius squared, ζ^2).

Second, the ripple contours whose variation is parallel to the ζ_x axis (i.e., those peaks and troughs which are parallel to ζ_z) arise predominately from the end disc of the cylinder. The spacing of the peaks and troughs in the ζ_x direction is an inverse function of the diameter of the end disc. The larger the diameter, the smaller the spacing. This can be compared to the more rapid fluctuations or smaller spacing between the peaks and troughs along the ζ_z direction which arise from the length of the cylinder.

Third, the scattering cross-section and its slope are zero at the origin. This is more easily seen in Figure 10 which corresponds to Figure 8 from a different viewing angle. Figure 10a is a logarithmic plot (in dB) while Figure 10b is a linear plot of the region near the origin which shows the zero value of the scattering cross-section and its slope. The region nearest the origin in wave space is known as the Rayleigh region. The scattering cross-section in this region increases approximately as the fourth power of the argument ζ . The rate of increase is related to the volume of the target. In our empirical model, it represents the "first moment" of the inclination factor. Consider the general expression for the structure factor, equation (40), for small values of the argument \vec{k} .

$$\begin{aligned}
 F(\vec{k} \rightarrow 0) &= \int \alpha(\vec{r}) \left[\frac{\vec{k} \cdot \hat{n}}{|\vec{k}|} \right] e^{i\vec{k} \cdot \vec{r}} dA(\vec{r}) \\
 &= \int \alpha(\vec{r}) \left[\frac{\vec{k} \cdot \hat{n}}{|\vec{k}|} \right] [1 + i\vec{k} \cdot \vec{r}] dA(\vec{r}) \quad . \quad (68)
 \end{aligned}$$

Thus

$$F(\vec{k} \rightarrow 0) = \int \alpha(\vec{r}) \left[\frac{\vec{k} \cdot \hat{n}}{|\vec{k}|} \right] dA(\vec{r}) + i \int \alpha(\vec{r}) \left[\frac{\vec{k} \cdot \hat{n}}{|\vec{k}|} \right] \vec{k} \cdot \vec{r} dA(\vec{r}) \quad (69)$$

For $\alpha(\vec{r}) = 1$, the first integral in equation (69) is a constant equal to the average value of the inclination factor. The second integral is proportional to $|\vec{k}|$, and, because of the \vec{r} factor in $\vec{k} \cdot \vec{r}$, represents what might be called the first moment of the inclination factor. Therefore, equation (69) can be written as:

$$F(\vec{k} \rightarrow 0) = C_0 + C_1 |\vec{k}| \quad (70)$$

(Text Continued on Page 39)

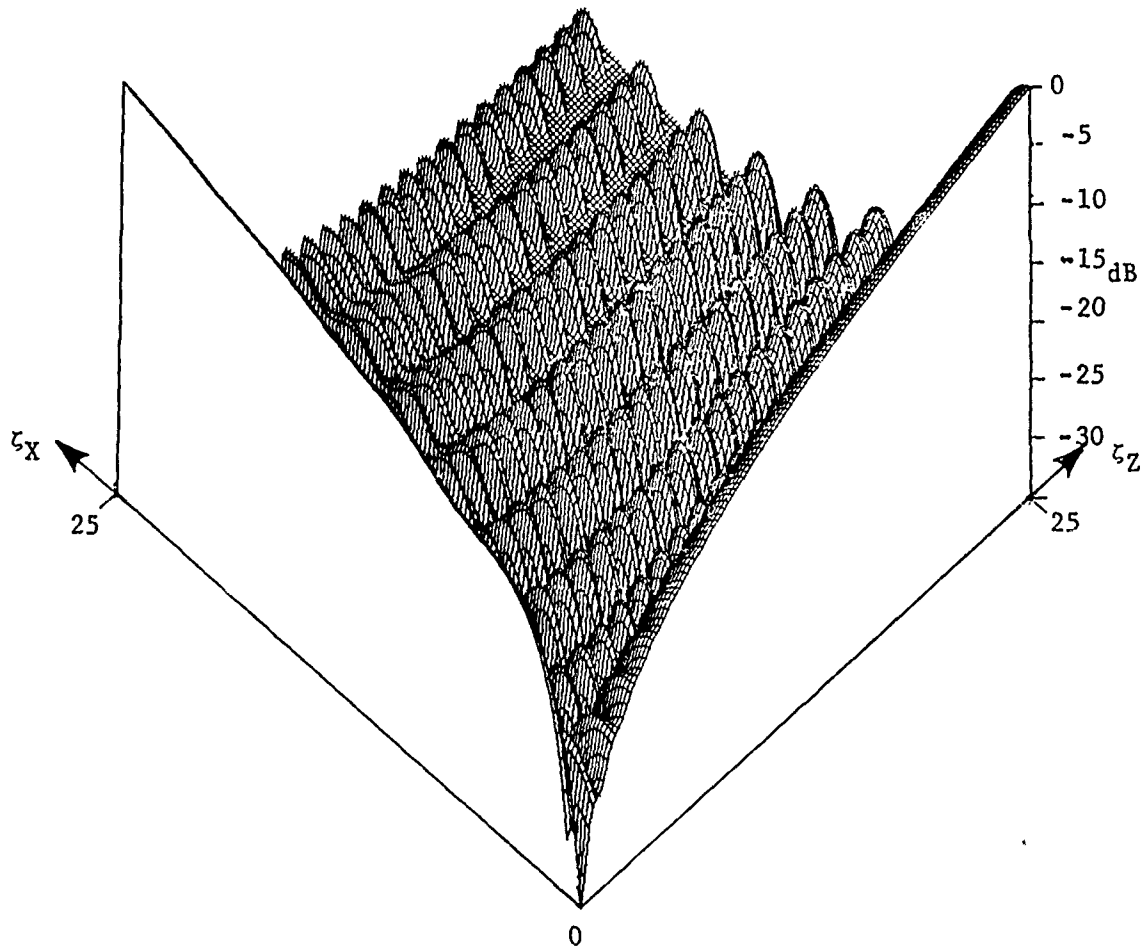


FIGURE 10a. ALTERNATE VIEW OF THE RIGID CYLINDER SCATTERING CROSS-SECTION (LOGARITHMIC ORDINATE)

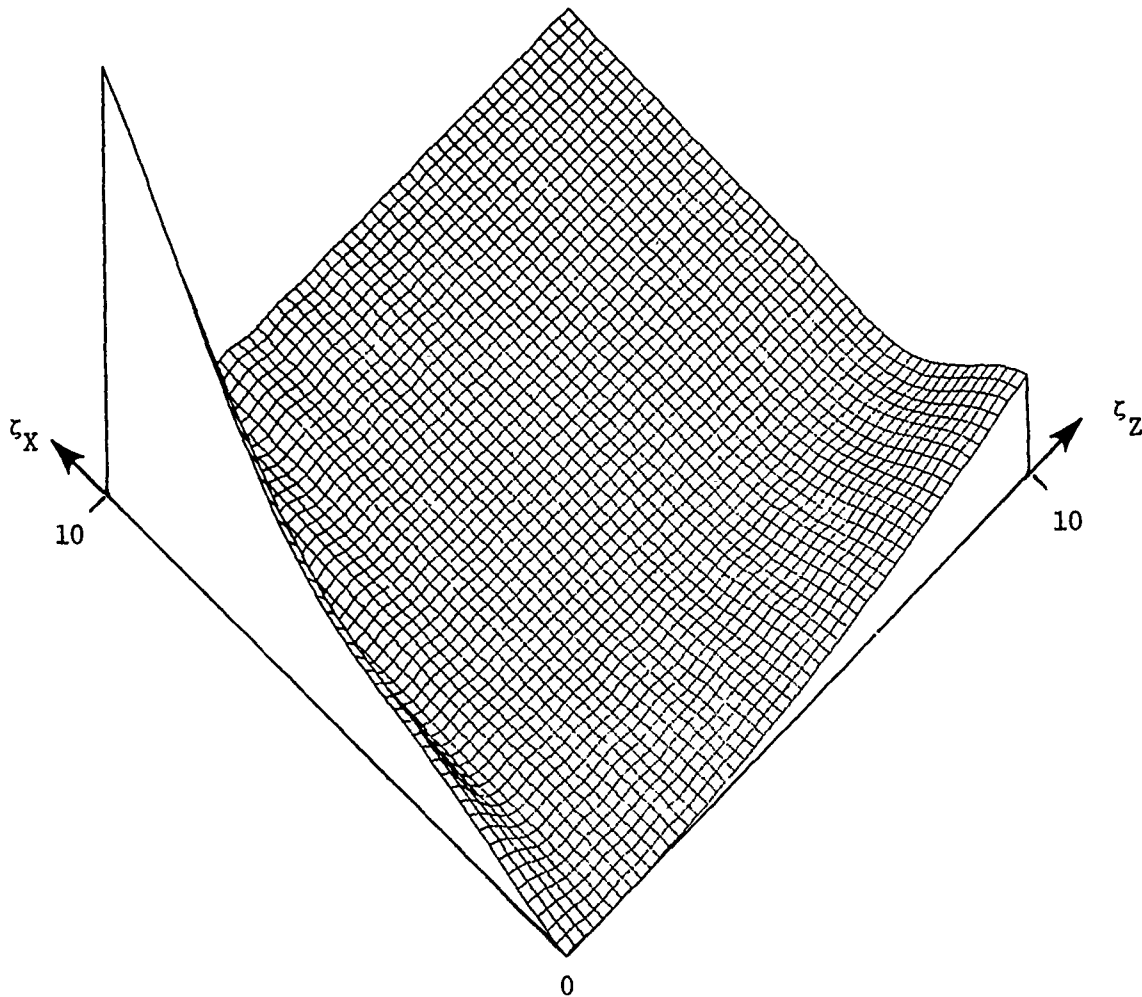


FIGURE 10b. LINEAR PLOT SHOWING THE RAYLEIGH REGION OF THE RIGID CYLINDER SCATTERING CROSS-SECTION

where C_0 is the zeroth moment or average value of the inclination factor and C_1 is the first moment. It can be argued that $C_1 \gg C_0$ since the moment arms are roughly equal to the average target-center to target-surface distance (compare, for example, the area of a spherical shell to the first moment of the area of a spherical shell). Thus,

$$[F(\vec{k} \rightarrow 0)]^2 = C_0^2 + 2C_0C_1|\vec{k}| + C_1^2|\vec{k}|^2 \quad (71)$$

or in terms of the dimensionless parameter ζ :

$$[F(\zeta \rightarrow 0)]^2 = C_0^2 + 2C_0C_1\zeta + C_1^2\zeta^2 \quad (72)$$

Therefore,

$$\Omega(\zeta \rightarrow 0) = C_0^2\zeta^2 + 2C_0C_1\zeta^3 + C_1^2\zeta^4 \quad (73)$$

From equation (73) we can see that the amplitude and slope of $\Omega(\zeta)$ at the origin are zero. For small values of the argument ζ , the behavior of $\Omega(\zeta)$ goes approximately as the fourth power of ζ because of the dominance of C_1 over C_0 .

For cases where $\alpha(\vec{r}) \neq 1$, our analysis obviously must be modified. For example, if $\alpha(\vec{r})$ can be approximated by a power series in "r," then the constants in equation (70) are the zeroth and first moments of the factor composed of the product $\alpha(\vec{r})$ and the inclination factor.

Returning to Figure 8, we note that except for the periodicity of the crests and troughs in the ζ_z and ζ_x directions and the behavior of $\Omega(\zeta)$ near the origin, there are few, if any, features of interest in the scattering cross section of the rigid, finite cylinder. This raises a subtle but important point. The plots, Figures 8 and 9, of the scattering cross section permit one, at a single glance, to note any significant features which might be of use in target classification. If features are present, their variation as a function of frequency and target

aspect can be noted easily. The probability that significant features are present for real targets appears high based upon results published in the literature.^{3,5} As we will see in Section VIII, incorporating impedance boundary conditions into our model is sufficient to produce interesting and significant features in the scattering cross-section of the finite cylinder. A collection of plots similar to Figure 8, but for a class of targets of interest, could be quite useful in the design of a sonar whose parameters (such as bandwidth and center frequency) are selected in order to optimize target classification or detection.

³ibid

⁵ibid

SECTION VII

IMPEDANCE BOUNDARY CONDITION

GENERAL CONSIDERATIONS

In order to develop a second level approximation to the model, one which incorporates the acoustic impedance properties of the target surface, let us consider the boundary conditions. Brekhovskikh¹⁹ has derived reflection and refraction coefficients for the case of a compressional plane wave in a fluid medium incident upon an infinite, plane, solid surface by solving the boundary value problem. The geometry and parameters are shown in Figure 11. The densities and wave speeds in the two media are indicated in the diagram. As Brekhovskikh shows, the incident, reflected, and refracted wave vectors all lie in a common plane (the X-Z plane in Figure 11) as a consequence of the boundary conditions. For an incident wave of unit amplitude, the complex amplitude of the wave reflected back into the fluid medium is:¹⁹

$$\alpha = \frac{Z_D \cos^2(2\theta_E) + Z_E \sin^2(2\theta_E) - Z_B}{Z_D \cos^2(2\theta_E) + Z_E \sin^2(2\theta_E) + Z_B} \quad (74)$$

where

$$Z_B = \frac{\rho_F c_F}{\cos \theta_B} ; Z_D = \frac{\rho_S c_D}{\cos \theta_D} ; Z_E = \frac{\rho_S c_E}{\cos \theta_E} \quad (75)$$

where the parameters are specified in Figure 11.

¹⁹Brekhovskikh, L. M., Waves in Layered Media, Academic Press, New York, 1960.

(Text Continued on Page 43)

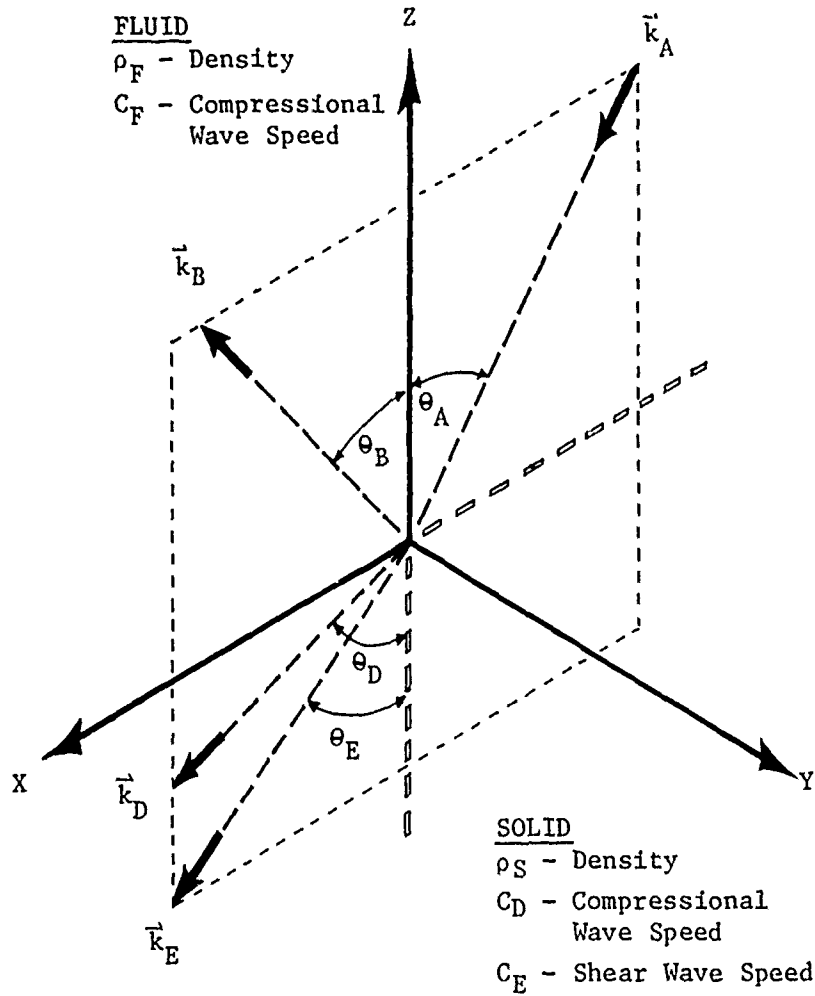


FIGURE 11. A COMPRESSIONAL PLANE WAVE, \vec{k}_A , IN A FLUID HALF SPACE IS REFLECTED FROM A FLUID-SOLID INTERFACE INTO THE DIRECTION \vec{k}_B AND REFRACTED INTO THE SOLID HALF SPACE IN THE FORM OF A COMPRESSIONAL WAVE, \vec{k}_D , AND A SHEAR WAVE, \vec{k}_E

The incident angle, θ_A , and reflection angle, θ_B , are equal while the refraction angles are found from a Snell's Law relation to be:

$$\theta_D = \sin^{-1} \left[\frac{C}{C_F} \sin \theta_A \right] \quad (76)$$

and

$$\theta_E = \sin^{-1} \left[\frac{C_E}{C_F} \sin \theta_A \right] . \quad (77)$$

The reflection coefficient, α , in equation (74) is a plane wave approximation and hence will fit nicely into the empirical model as a surface distribution coefficient to be used with the inclination factor. This will permit a second level approximation for scattering from a finite cylinder providing the form of equation (74) can be modified to correspond to the parameters used for expressing the structure factor, equation (40). The only parameter in equation (74) which must be expressed in wave-space and real-space parameters is θ_A , the incidence angle, since $\theta_B = \theta_A$ and θ_D and θ_E may be derived via equations (76) and (77). The angle of incidence, for a specific differential area element, can be found by considering the inclination factor and by referring to Figure 4.

$$\frac{\vec{k} \cdot \hat{n}}{|\vec{k}|} = \hat{k} \cdot \hat{n} = \cos \theta_A \quad (78)$$

where θ_A is the angle of incidence and \hat{n} is the normal to the differential area element. Equation (78) applies equally to the hemi-cylinder surface as well as the end disc. The form of α is different, however, for the end disc versus the hemi-cylinder when expressed in wave space and real space parameters because of the difference in orientation of the surfaces with respect to a given \vec{k} direction.

END DISC REFLECTION COEFFICIENT

Referring to Figure 5, the end disc, S_1 , is a planar surface. Thus, the unit normals for all differential area elements point in the same direction. This means that the reflection coefficient, equation (74), is independent of the integration variable and can be taken outside the integral of equation (40), i.e.;

$$F_{S_1}(\vec{k}) = \alpha_1 \int_{S_1} \frac{\vec{k} \cdot \hat{n}}{|\vec{k}|} e^{i\vec{k} \cdot \vec{r}} dA_1(\vec{r}) . \quad (79)$$

The form of α_1 for the end plate will be derived for the back-scattering case only. The bistatic case has been investigated qualitatively and appears to be different. The implication of this difference appears contrary to the principle of reciprocity but is still under consideration.

For the end disc:

$$\frac{\vec{k} \cdot \hat{n}}{|\vec{k}|} = \frac{k_z}{|\vec{k}|} = \cos \theta_{A_1} . \quad (80)$$

Recalling the restriction, described earlier, that both \vec{k}_1 and \vec{k}_2 are coplanar with the cylinder axis (hence, they define the k_z - k_x plane), we know that:

$$|\vec{k}|^2 = k_x^2 + k_z^2 . \quad (81)$$

Therefore,

$$\sin \theta_{A_1} = [1 - \cos^2 \theta_{A_1}]^{\frac{1}{2}}$$

$$\begin{aligned}
 &= \left[1 - \left(\frac{k_z}{|\vec{k}|}\right)^2\right]^{\frac{1}{2}} \\
 &= \frac{k_x}{|\vec{k}|} .
 \end{aligned} \tag{82}$$

Equation (82) can be used with equations (76) and (77) and familiar trigonometric double angle formulae to specify all the parameters in equation (40) for the reflection coefficient. The results are listed below.

$$z_{B_1} = \frac{\rho_F C_F |\vec{k}|}{k_z} , \tag{83}$$

$$z_{D_1} = \rho_S C_D \left[1 - \left(\frac{C_D k_x}{C_F |\vec{k}|}\right)^2\right]^{-\frac{1}{2}} , \tag{84}$$

$$z_{E_1} = \rho_S C_E \left[1 - \left(\frac{C_E k_x}{C_F |\vec{k}|}\right)^2\right]^{-\frac{1}{2}} , \tag{85}$$

$$\sin^2(2\theta_{E_1}) = \left(\frac{2C_E k_x}{C_F |\vec{k}|}\right)^2 \left[1 - \left(\frac{C_E k_x}{C_F |\vec{k}|}\right)^2\right] , \tag{86}$$

$$\cos^2(2\theta_{E_1}) = \left[1 - 2\left(\frac{C_E k_x}{C_F |\vec{k}|}\right)^2\right]^2 . \tag{87}$$

Equations (83)-(87) may be substituted into equation (74) to produce the reflection coefficient, α_1 , for the cylinder end disc. The second level approximation for the end disc structure factor is found using equation (50):

$$F_{S_1}(\vec{k}) = (\alpha_1)(2\pi a^2 e^{ik_z L/2}) \frac{k_z}{|\vec{k}|} \left[\frac{J_1(k_x a)}{k_x a} \right] . \quad (88)$$

HEMI-CYLINDER REFLECTION COEFFICIENT

The case of the hemi-cylinder reflection coefficient is more difficult because α_2 depends upon the integration variable. Recalling the cylinder orientation and the parameters shown in Figures 5 and 7, it is obvious that the inclination factor varies along the arc length curvature but not in the direction of the cylinder or z-axis. Hence, we pick a representative point, P, on the hemi-cylinder surface to be in the X-Y plane as shown in Figure 12.

The angle between the scattering vector, \vec{k} , and the unit normal, \hat{n} , as specified in equation (78), is θ_A as shown in Figure 12. However, the wave-space and real-space parameters k_x , k_z , x , and z can be expressed directly in terms of the integration angle, ϕ , and the angle θ_1 in Figure 12.

$$\frac{\vec{k} \cdot \hat{n}}{|\vec{k}|} = \cos \theta_A . \quad (89)$$

But from spherical trigonometry we have the relation:

$$\cos \theta_A = \cos \phi \cos \theta_1 . \quad (90)$$

From Figure 12, we see that:

$$\cos \phi = \frac{x}{a} \quad (90a)$$

(Text Continued on Page 48)

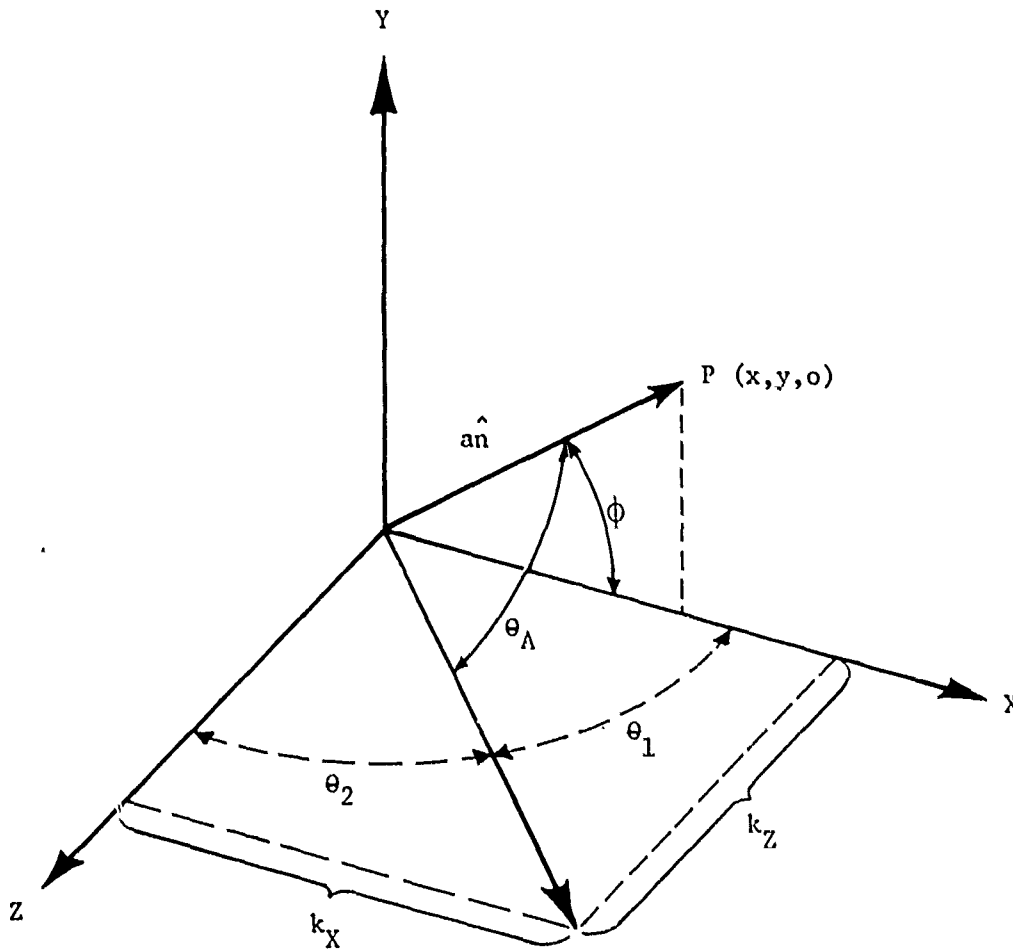


FIGURE 12. RELATIONSHIP BETWEEN THE SCATTERING VECTOR \vec{k} AND THE VECTOR $(\hat{a}n)$ NORMAL TO THE HEMI-CYLINDER SURFACE AT THE POINT $P(x, y, 0)$

and

$$\cos \theta_1 = \frac{k_x}{|\vec{k}|} \quad (90b)$$

Thus,

$$\cos \theta_A = \frac{k_x x}{|\vec{k}| a} \quad (91)$$

Equation (91) may be used with equations (76) and (77) and the double angle formulae to provide expressions similar to equations (83)-(87) for the cylinder side surface. The results are:

$$Z_{B_2} = \frac{\rho_F C_F |\vec{k}| a}{k_x x} \quad (92)$$

$$Z_{D_2} = \rho_S C_D \left\{ 1 - \left(\frac{C_D}{C_F} \right)^2 \left[1 - \left(\frac{k_x x}{|\vec{k}| a} \right)^2 \right] \right\}^{-\frac{1}{2}} \quad (93)$$

$$Z_{E_2} = \rho_S C_E \left\{ 1 - \left(\frac{C_E}{C_F} \right)^2 \left[1 - \left(\frac{k_x x}{|\vec{k}| a} \right)^2 \right] \right\}^{-\frac{1}{2}} \quad (94)$$

$$\sin^2(2\theta_{E_2}) = \left(\frac{2C_E}{C_F} \right)^2 \left[1 - \left(\frac{k_x x}{|\vec{k}| a} \right)^2 \right] \cdot \left\{ 1 - \left(\frac{C_E}{C_F} \right)^2 \left[1 - \left(\frac{k_x x}{|\vec{k}| a} \right)^2 \right] \right\} \quad (95)$$

and

$$\cos^2(2\theta_{E_2}) = \left\{ 1 - 2 \left(\frac{C_E}{C_F} \right)^2 \left[1 - \left(\frac{k_x x}{|\vec{k}| a} \right)^2 \right] \right\}^2 \quad (96)$$

for the curved side surface of the cylinder.

HEMI-CYLINDER STRUCTURE FACTOR

The structure factor for the hemi-cylinder surface, S_2 , may be written by modifying equation (55) to include the reflection coefficient, $\alpha_2(x)$, for the side surface:

$$F_{S_2}(\vec{k}) = \frac{2k_x L}{|\vec{k}|} \left[\frac{\sin\left(\frac{k_z L}{2}\right)}{\frac{k_z L}{2}} \right] \left[\int_0^a \frac{\alpha_2(x) x e^{ik_x x}}{(a^2 - x^2)^{\frac{1}{2}}} dx \right] \quad (97)$$

where $\alpha_2(x)$ is given by equation (74) with the aid of equations (92)-(96). Equation (97) must be evaluated by numerical integration.

COMPLEX VALUES OF THE REFLECTION COEFFICIENTS

The reflection coefficients α_1 and $\alpha_2(x)$ in equations (88) and (97), in general, are complex. For incident angles θ_A , in equations (76) and (77), which are less than the critical angle for compressional and shear waves, i.e.,

$$\sin \left[\frac{C}{C_{F,E}} \sin \theta_A \right] \leq 1 \quad (98)$$

the reflection coefficients are real. For θ_A greater than either critical angle, the reflection coefficients are complex; i.e., real plus imaginary. In order to evaluate the reflection coefficients in these complex domains, the refraction angles, θ_D and θ_E , were expressed in terms of complex components:

$$\theta_j = \gamma_j + i \beta_j, \quad j = B \text{ or } E. \quad (99)$$

Thus, the Snell's law relations, equations (76) and (77), take the form:

$$\sin \theta_j = \sin \gamma_j = \frac{C_j}{C_F} \sin \theta_A \quad (100)$$

$$(\text{for } \gamma_j \leq \pi/2; \beta_j = 0)$$

and

$$\sin \theta_j = \cosh \beta_j = \frac{C_j}{C_F} \sin \theta_A \quad (101)$$

$$(\text{for } \gamma_j = \pi/2; \beta_j > 0) .$$

The relations to be used in the reflection coefficient for θ_A greater than the critical angle are:

$$Z_j = -i\rho_j C_j (\sinh \beta_j)^{-1} , \quad (102)$$

$$\sin^2(2\theta_j) = -\sinh^2(2\beta_j) , \quad (103)$$

and

$$\cos^2(2\theta_j) = \cosh^2(2\beta_j) , \quad (104)$$

where

$$\beta_j = -\left| \cosh^{-1} \left[\left(\frac{C_j}{C_F} \right) \sin \theta_A \right] \right| . \quad (105)$$

The reflection coefficient, α , in equation (74) depends upon the densities of the fluid and solid (ρ_F and ρ_S), the compressional wave speed in the fluid (C_F), and the compressional and shear wave speeds (C_D and C_E) in the solid, as well as the angle of incidence, θ_A . The moduli and phase angles of the reflection coefficients for brass and aluminum planar surfaces in water are shown in Figures 13 and 14, respectively. The modulus and phase for an aluminum surface in air are shown in Figure 15.

(Text Continued on Page 54)

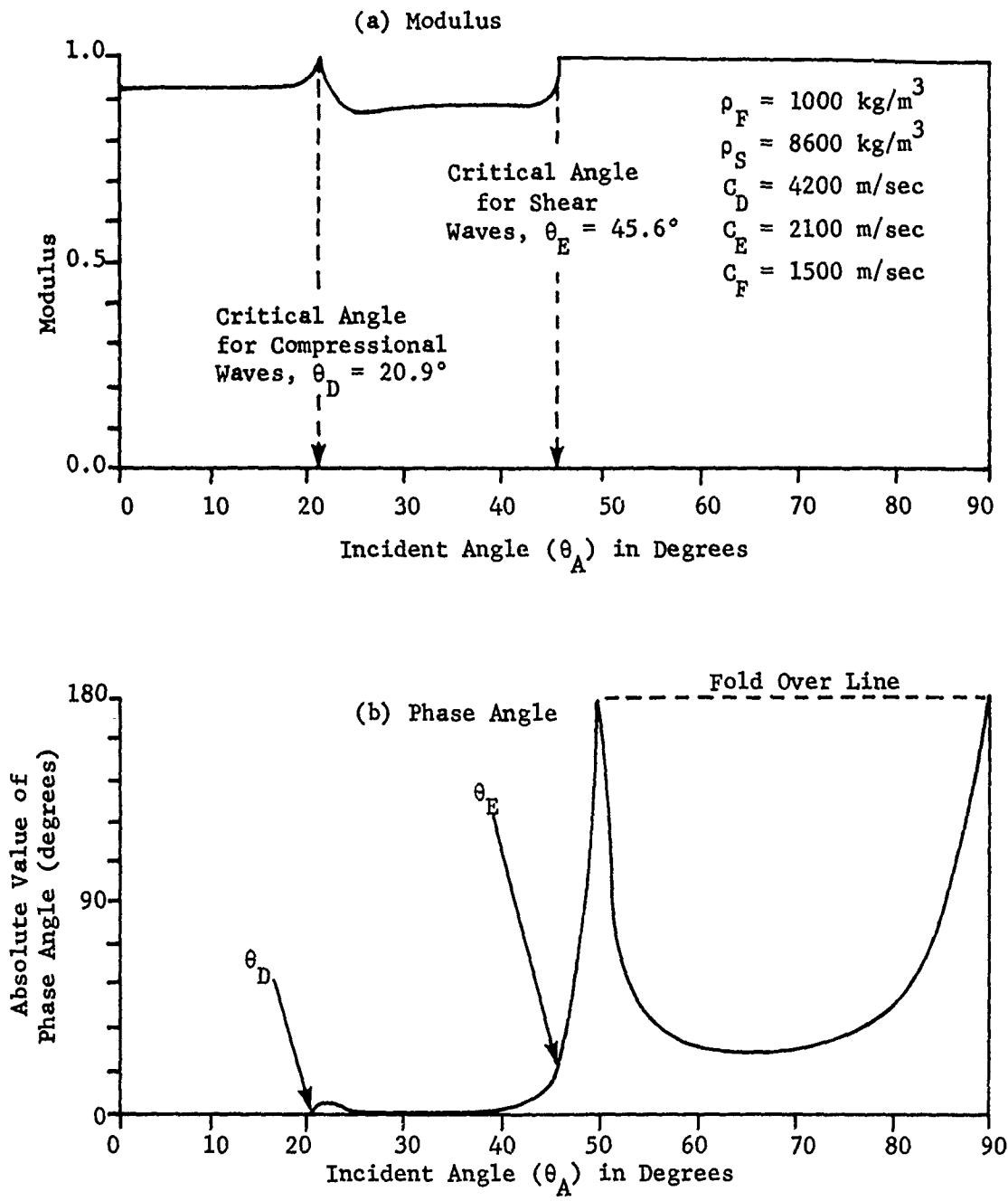


FIGURE 13. REFLECTION COEFFICIENT (a) MODULUS, AND (b) PHASE ANGLE FOR BRASS IN WATER

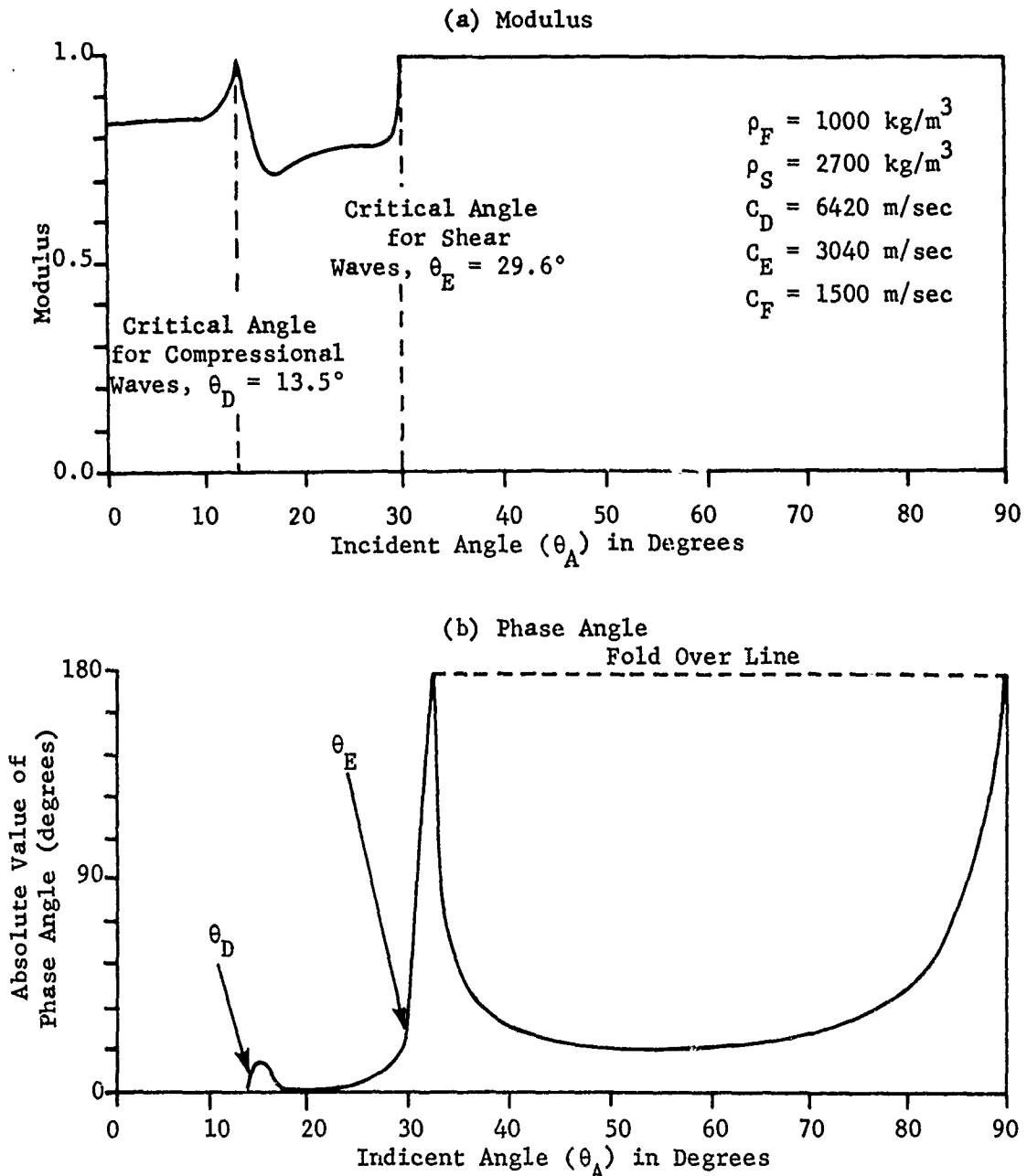


FIGURE 14. REFLECTION COEFFICIENT (a) MODULUS, AND (b) PHASE ANGLE FOR ALUMINUM IN WATER

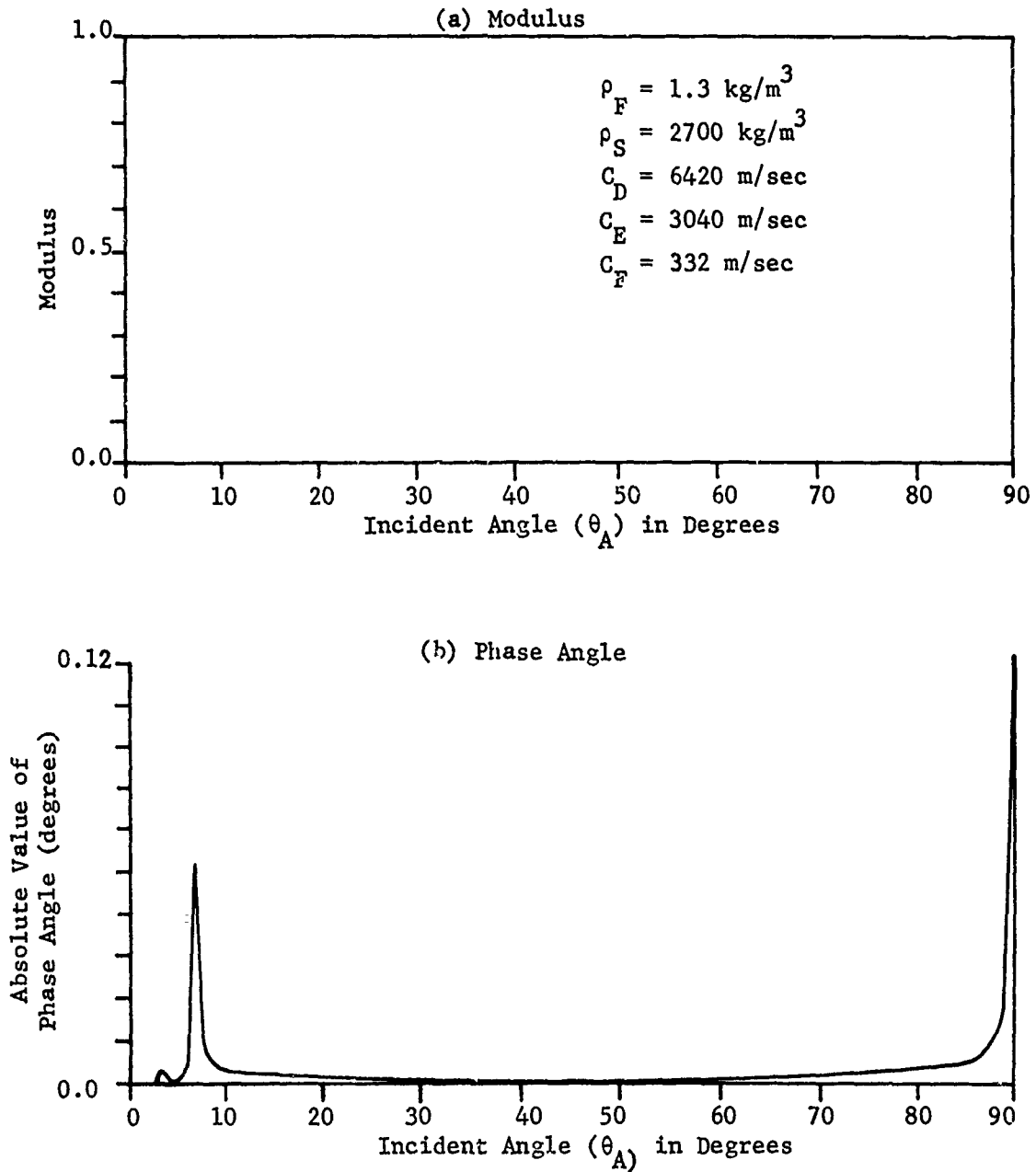


FIGURE 15. REFLECTION COEFFICIENT (a) MODULUS, AND (b) PHASE ANGLE FOR ALUMINUM IN AIR

The moduli for brass and aluminum in water are similar in character. Each has a small cusp at the critical angle for compressional waves in the solid, followed by a shallow trough which rises to unity at the critical angle for shear waves in the solid. Phase angle plots are for the absolute value of the phase angle. Hence, the large cusps in the phase angle plots are artifacts which arise from the folding of values in the range 180 degrees - 360 degrees back into the range 180 degrees - 0 degrees about the 180 degree line. The smaller bumps in the phase angle plots occur at the compressional critical angle while the nearly 360 degree phase shifts (large artifact cusps) occur at the critical angle for shear waves.

The aluminum plane in air, Figure 15, is characterized by a reflection coefficient whose modulus is unity for all incidence angles and whose phase is essentially zero everywhere. This could be anticipated since the ratio of the densities of the two media is so large. Thus, the case of aluminum in air should approximate, very closely, a rigid scatterer. Indeed, this case was used to test the algorithm for computing the scattering from an elastic cylinder via the reflection coefficients as outlined previously. The results are presented in the next section.

SECTION VIII

IMPEDANCE CYLINDER SCATTERING CROSS SECTION

The boundary conditions discussed in Section VII can be expected to affect the dimensionless scattering cross-section, $\Omega(\zeta)$, for a finite cylinder providing the densities and wave speeds in the two media are sufficiently different. Variations in $\Omega(\zeta)$ due to the scattering amplitude can be expected to be moderate when no dramatic variation is observed in the modulus of the reflection coefficient (See Figures 13a and 14a for brass and aluminum in water). However, the phase variations which occur at the critical angles for compressional and shear waves can be expected to have a dramatic impact since they affect the manner in which two or more scattered waves interfere. This hypothesis suggests that the shear critical angle will be the dominant parameter because of the abrupt 2π phase shift. This is consistent with Hickling's² results which indicate that the spacing between peaks in the experimental frequency response for elastic spheres is most strongly correlated with the shear wave speed.

The scattering cross-section for a finite, elastic cylinder with a length to radius ratio of 6 was calculated using the end disc and hemicylinder structure factors given by equations (88) and (97). Evaluation of the integral in equation (97) was accomplished by numerical methods.

Three examples were investigated. First, $\Omega(\zeta)$ was calculated for an aluminum cylinder in air. The parameters were the same as those specified in Figure 15. The purpose of this example was to test the computer algorithm. In principal, the results should be the same as those for the rigid cylinder. Comparison of the scattering cross-section for the aluminum cylinder in air, Figure 16, with that of the rigid cylinder, Figure 8, indicates that this is, indeed, the case.

(Text Continued on Page 57)

²ibid

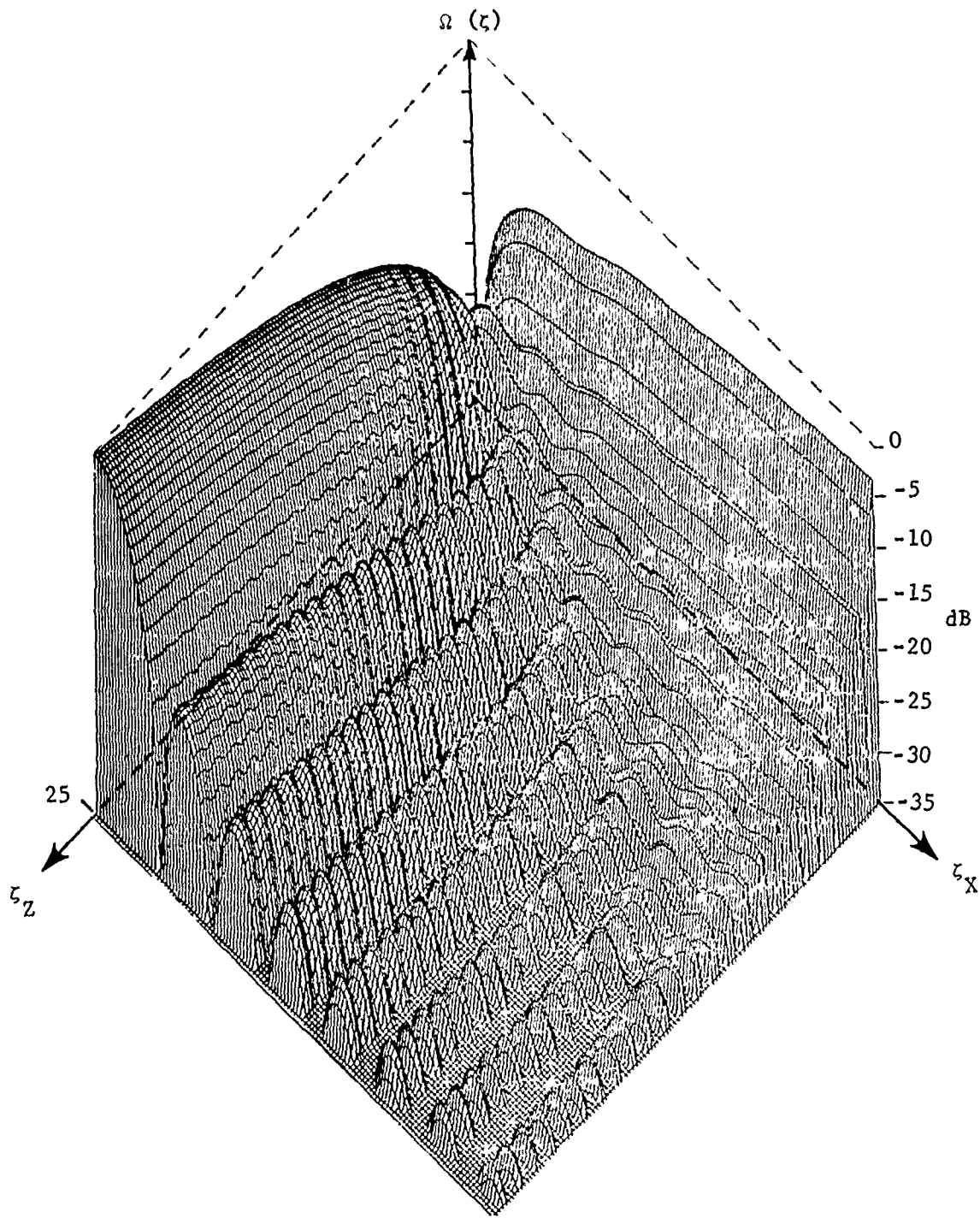


FIGURE 16. SCATTERING CROSS-SECTION FOR AN ALUMINUM CYLINDER IN AIR

The scattering cross-section for the aluminum cylinder in water was calculated using the parameters given in Figure 14. A three-dimensional plot of $\Omega(\zeta)$ is shown in Figure 17. A second plot, shown in Figure 18, has been rotated 180° from that shown in the previous figure. A black and white contour plot showing all four quadrants is given in Figure 19. Several significant features are clearly visible in Figure 17. First, a single broad trough extends from $\zeta_x = 10$ outward at approximately 30 degrees from the ζ_x axis. This corresponds to the critical angle for shear waves with respect to the side surface of the cylinder. The breadth of the trough is believed to be due to the variation of the shear critical angle caused by the curvature of the side surface.

A much more subtle effect is observed for the cylinder end disc. A faint ridgeline can be seen running from near the origin diagonally across the maximum which is parallel to the ζ_2 axis. This ridgeline is approximately 15 degrees from the ζ_2 axis. It arises from the small, sharp peak in the reflectivity curve, Figure 14a, which corresponds to the critical angle for compressional waves in aluminum. No broad minimum at the critical angle (30 degrees) for shear waves into the end disc is apparent. Presumably this is absent for two reasons: (1) the critical angle is sharp; (2) all points on the surface of the end disc pass through the critical angle simultaneously so that no new destructive or constructive interference occurs between various parts of the end disc. Since the critical angles for the end disc and the curved side surface do not overlap, no significant cross interference between the contributions of these two components is manifested. That is, because the amplitude of one component is small in the vicinity of the shear critical angle of the other component, intensity fluctuations caused by cross interference are very small.

Another subtle feature in the scattering cross-section for aluminum in water is the shallow, broad minimum in the ridgeline along the ζ_x

(Text Continued on Page 61)

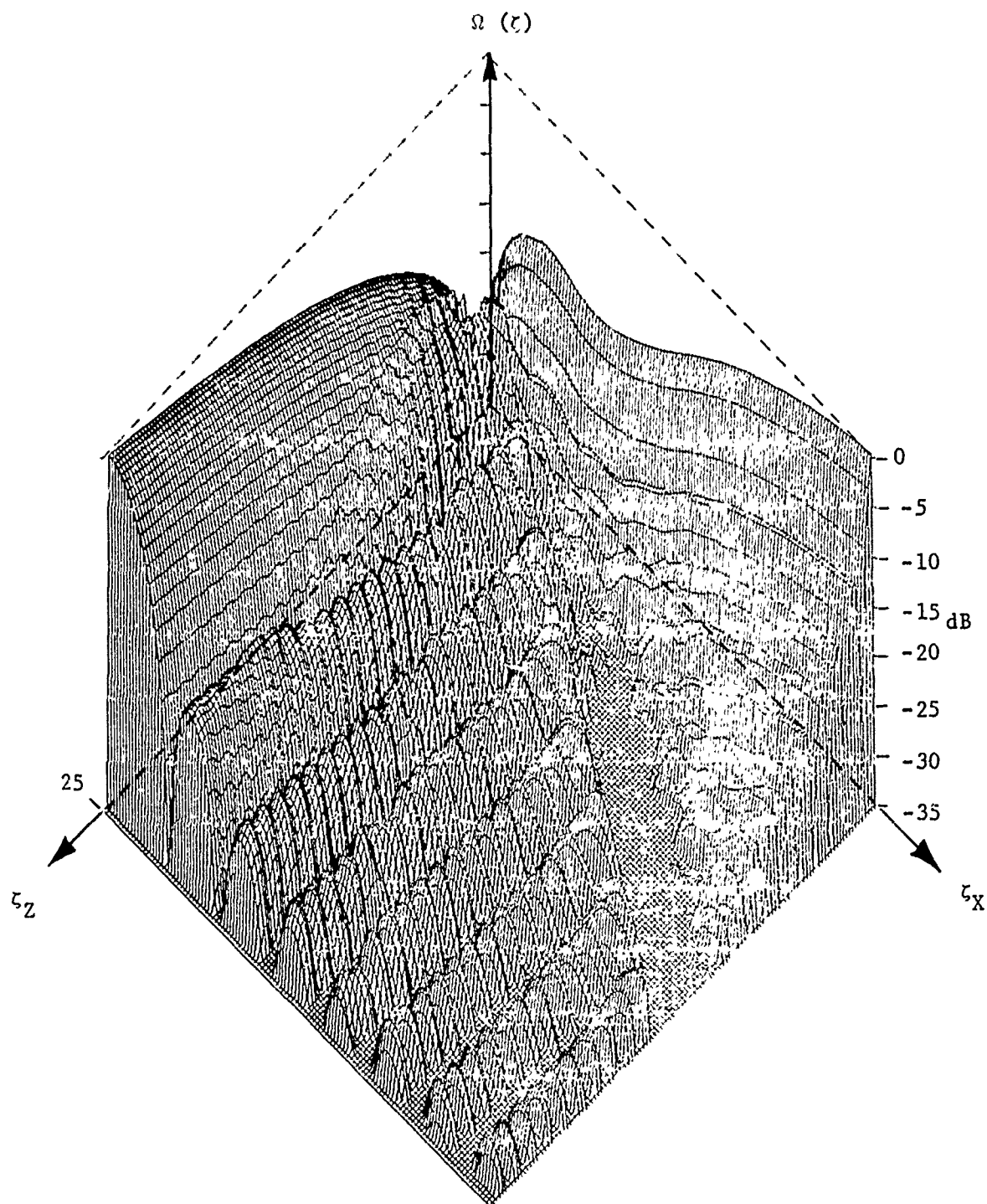


FIGURE 17. SCATTERING CROSS-SECTION FOR AN ALUMINUM CYLINDER IN WATER

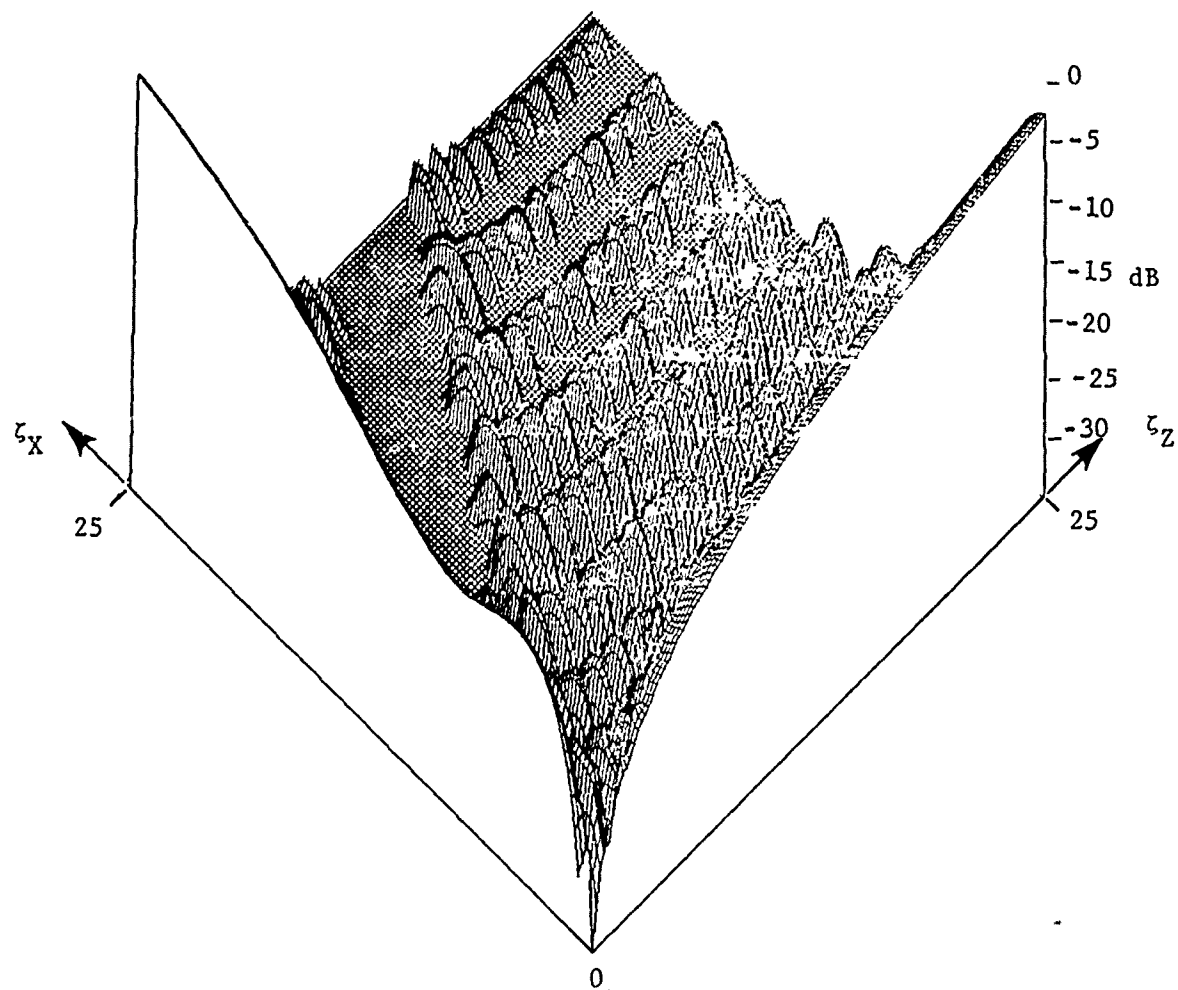


FIGURE 18. ALTERNATE VIEW OF THE SCATTERING CROSS-SECTION FOR AN ALUMINUM CYLINDER IN WATER

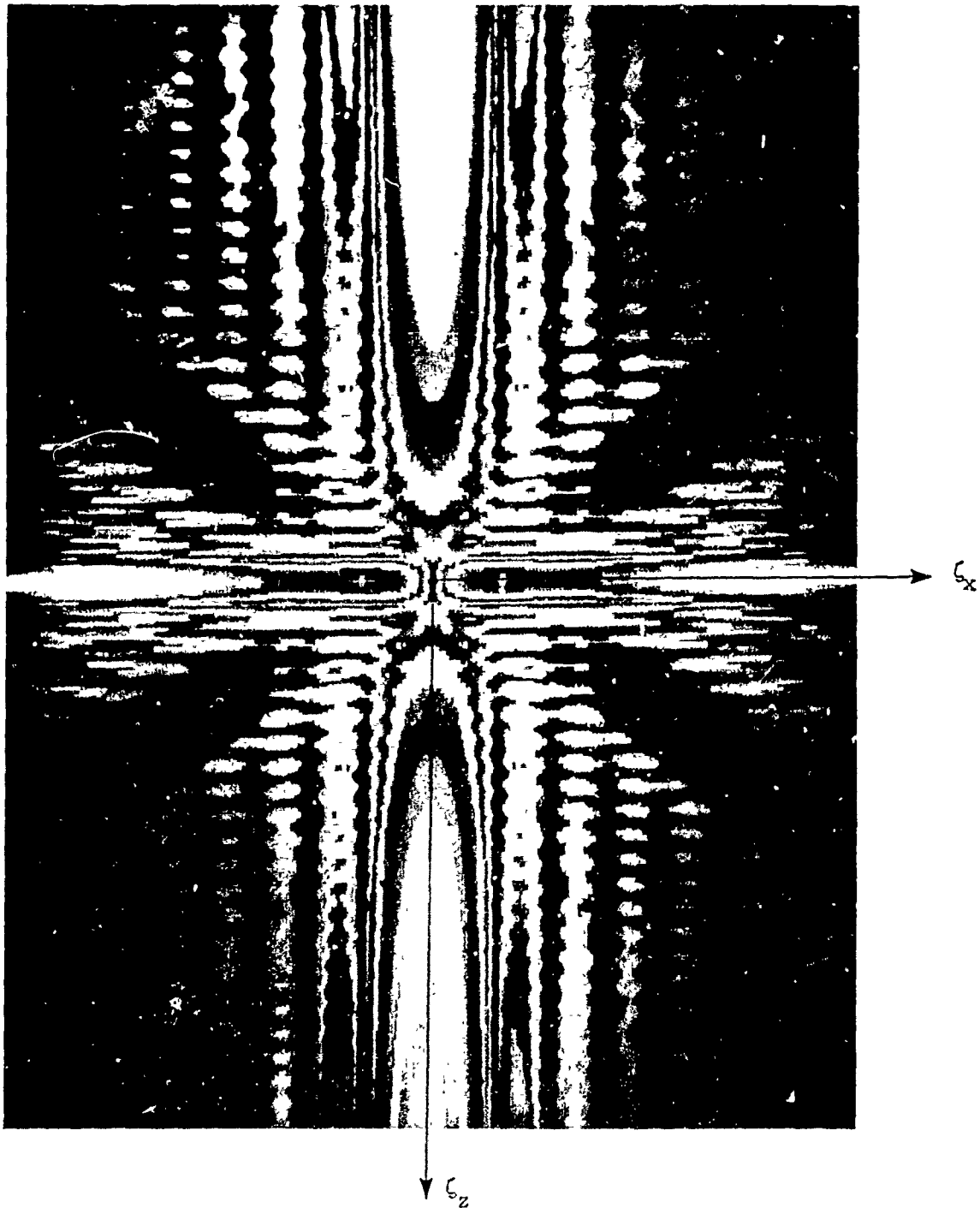


FIGURE 19. SHADED CONTOUR PLOT OF THE SCATTERING CROSS-SECTION FOR AN ALUMINUM CYLINDER IN WATER

axis. It is believed that this minimum is coupled to the flat region at 30 degrees arising from shear wave effects and that it will show oscillatory behavior with a complementing flat region when the scattering cross-section is computed to larger values for ζ_x than those shown in Figure 17. One final point can be made. Since the approximation utilized for these calculations does not take into account energy which penetrates the surface and is scattered out again, the region in Figure 17 from 30 degrees to 60 degrees, measured from the ζ_z axis, is beyond the critical angles for both the end disc and all portions of the curved side surface. Thus, the response in this region should be the same as that for the rigid cylinder. Comparison of Figures 17 and 8 confirms this. Inspection of Figures 18 and 19 reveals no additional features of interest for the aluminum cylinder in water. However, these additional representations do help to clarify points already described.

The scattering cross-section for a brass cylinder in water is presented in Figures 20, 21, and 22. The parameters used in the evaluation were the same as those shown in Figure 13a. In contrast to aluminum, the shear critical angle for brass is approximately 45 degrees. Hence one might anticipate that there would be strong cross interference effects. The spotty minimum which runs at 45° to the ζ_z axis in Figure 20 is believed to arise from this cross interference between the end disc and hemi-cylinder.

There is only a faint hint of a ridgeline arising from the peak in the reflectivity curve at 21 degrees to the end disc near the origin in Figure 20. This diminished effect is in agreement with the difference in the reflectivity peaks in Figures 13a and 14a. The beginning of a broad, flat minimum at the bottom right of Figure 20 also is apparent. It is believed that this is the second oscillation of shear effects mentioned earlier with regard to Figure 17.

Although the scattering cross-sections presented in this section are not expected to describe experimental data accurately, they do represent an improvement over the rigid cylinder approximation.

(Text Continued on Page 65)

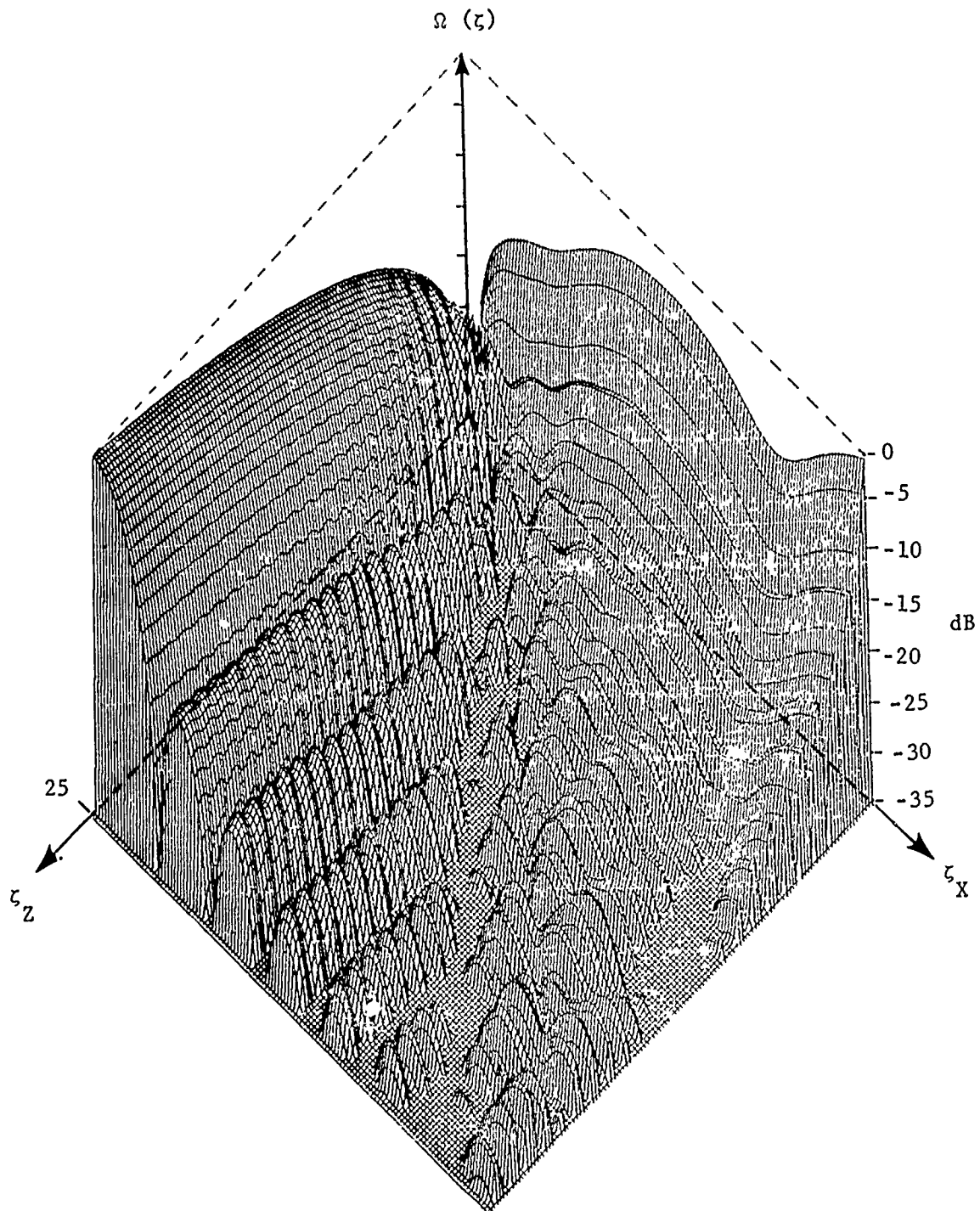


FIGURE 20. SCATTERING CROSS-SECTION FOR A BRASS CYLINDER IN WATER

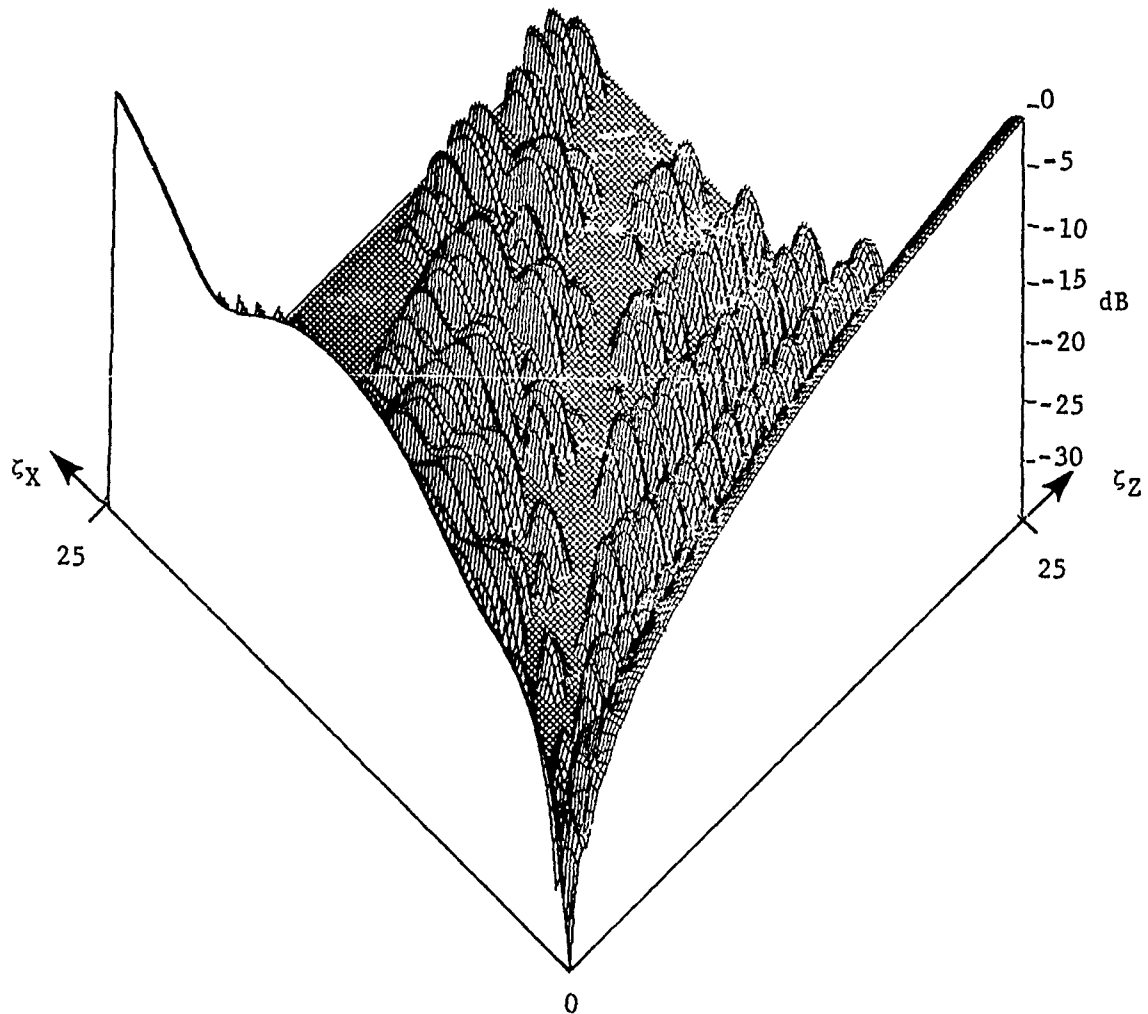


FIGURE 21. ALTERNATE VIEW OF THE SCATTERING CROSS-SECTION FOR A BRASS CYLINDER IN WATER

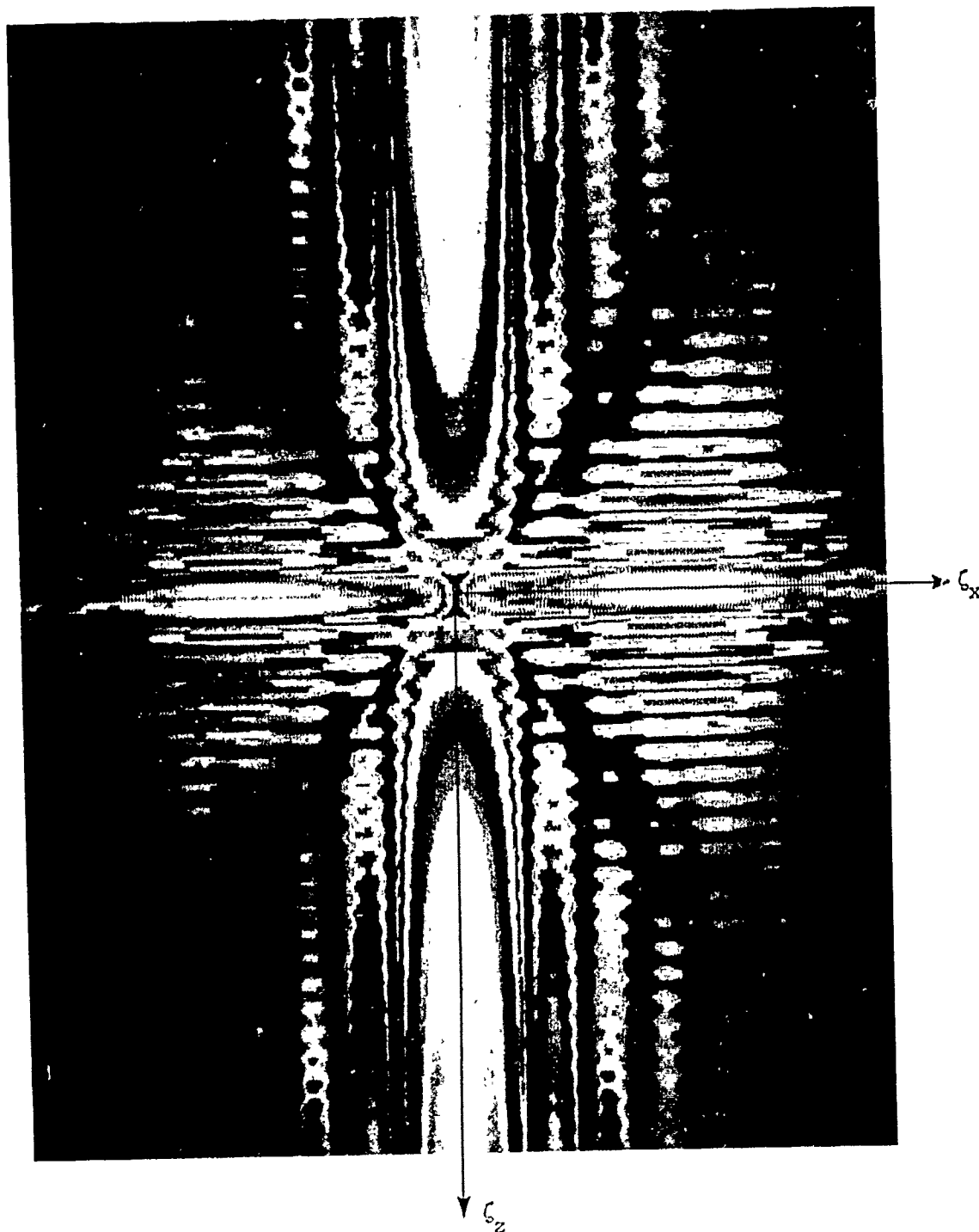


FIGURE 22. SHADED CONTOUR PLOT OF THE SCATTERING CROSS-SECTION FOR A BRASS CYLINDER IN WATER

Additionally, they dramatize the significance of the role of the boundary conditions in determining the nature of the scattering cross-section of any target. This may be fortuitous if a simple set of target indicators is sought which emphasizes universal boundary effects. On the other hand, if geometry indicators are sought, it may represent a severe complexity.

SECTION IX

SUMMARY AND CONCLUSIONS

Starting from the wave equation, an empirical plane wave model for acoustic target scattering has been developed. The model employs plane waves and represents the total scattered field as a sum of contributing effects called structure factors. The principal benefit of this model is that it provides a formalism for simultaneously representing both the frequency and the aspect dependence of the target response in terms of a vector parameter in wave-space. The relationships between the wave-space and real-space parameters have been described so that features which are observed in the target's scattering cross-section in wave-space can be related to real-space parameters such as target geometry, orientation and boundary conditions. This formalism can be utilized not only for further refinements of the empirical model but also as a means for graphically displaying experimental data. In this way, it is hoped that interpretation of experimental measurements will be facilitated by familiarity with similar displays of model results.

The model was applied to scattering from a right circular cylinder of finite length. This cylinder is of interest because it is a mine-like target and because it has a non-analytic surface; that is, it has sharp edges. It is these edges which make empirical modeling a viable approach to the acoustic scattering problem because sophisticated theoretical models break down when mathematical discontinuities are encountered. A concise mathematical relation was derived for the structure factor for the right circular cylinder with rigid boundary conditions. Elastic boundary conditions were examined and incorporated into the model. Because of the complexity of the mathematics for the elastic case, a concise mathematical expression was not possible. Evaluation of the structure factor for the cylinder with elastic boundary conditions required a numerical integration by computer. One effect was to

increase the computer computation time for evaluation of the scattering cross-section by a factor of 32.

Comparison of the scattering cross-section for the cylinder with different boundary conditions indicated dramatic differences. Although no account yet has been taken of waves internally scattered within the target, the results to date indicate that variations in boundary conditions alone can produce markedly different scattering results for the same target shape. When internal scattering is included, it is anticipated that these differences will increase rather than dissipate.

INITIAL DISTRIBUTION LIST

054	Chief of Naval Research	
	(Code 480)	(Copy 1)
	(Code 480T)	(Copy 2)
	(Code 485)	(Copy 3)
	(Code 486)	(Copy 4)
	(Code 460T)	(Copy 5)
	(Code 463)	(Copy 6)
	(Code 210)	(Copy 7)
	(Code 212)	(Copy 8)
	(Code 220)	(Copy 9)
	(Code 222)	(Copy 10)
003	Chief of Naval Operations	
	(OP-951F)	(Copy 11)
	(OP-009T)	(Copy 12)
	(OP-323)	(Copy 13)
	(OP-374)	(Copy 14)
	(OP-374T)	(Copy 15)
	(OP-981F)	(Copy 16)
	(OP-353C)	(Copy 17)
	(OP-395C)	(Copy 18)
162	Commander, Naval Air Systems Command	
	(AIR 5305)	(Copy 19)
	(AIR 53052)	(Copy 20)
193	Commander, Naval Electronic Systems Command	
	(PME 124R)	(Copy 21)
	(PME 3203)	(Copy 22)
	(NELEX 320)	(Copy 23)
	(NELEX 320A)	(Copy 24)
001	Chief of Naval Material	
	(MAT 08T2)	(Copy 25)
	(MAT 08T2B)	(Copy 26)
	(MAT 08T21)	(Copy 27)
427	Commander, Naval Sea Systems Command	
	(SEA 63)	(Copy 28)
	(SEA 63R)	(Copy 29)
	(SEA 63R1)	(Copy 30)
	(SEA 63R11)	(Copy 31)
	(SEA 63R3)	(Copy 32)
	(SEA 63D-7)	(Copy 33)
	(SEA 06H1)	(Copy 34)
	(SEA 06H1-1)	(Copy 35)
	(SEA 660)	(Copy 36)
	(SEA 660-CL)	(Copy 37)
	(SEA 660-7)	(Copy 38)
	(PMS 407)	(Copy 39)
	(PMS 4075)	(Copy 40)
	(PMS 40771)	(Copy 41)
265	Commander, Naval Ocean Systems Center	
	(Code 52)	(Copy 42)
	(Code 5213)	(Copy 43)
	(Code 623)	(Copy 44)
692	Director, Hawaii Laboratory, Naval Ocean Systems Center, Kailua	
	(Code 510E)	(Copy 45)
	(Code 512)	(Copy 46)
277	Commander, Naval Underwater Systems Center	
	(Code 32)	(Copy 47)
075	Director, Defense Technical Information Center	(Copies 48-59)